Article

Surface Reaction Kinetics of Steam- and CO$_2$-Reforming as Well as Oxidation of Methane over Nickel-Based Catalysts

Karla Herrera Delgado [1], Lubow Maier [2], Steffen Tischer [2], Alexander Zellner [1], Henning Stotz [1] and Olaf Deutschmann [1,2,*]

[1] Institute for Chemical Technology and Polymer Chemistry, Karlsruhe Institute of Technology (KIT), 76128 Karlsruhe, Germany; E-Mails: karla.delgado@kit.edu (K.H.D.); alexander.zellner@kit.edu (A.Z.); henning.stotz@kit.edu (H.S.)

[2] Institute for Catalysis Research and Technology, Karlsruhe Institute of Technology (KIT), 76128 Karlsruhe, Germany; E-Mails: lubow.maier@kit.edu (L.M.); steffen.tischer@kit.edu (S.T.)

* Author to whom correspondence should be addressed; E-Mail: olaf.deutschmann@kit.edu; Tel.: +49-721-608-43064.

Academic Editor: Keith Hohn

Abstract: An experimental and kinetic modeling study on the Ni-catalyzed conversion of methane under oxidative and reforming conditions is presented. The numerical model is based on a surface reaction mechanism consisting of 52 elementary-step like reactions with 14 surface and six gas-phase species. Reactions for the conversion of methane with oxygen, steam, and CO$_2$ as well as methanation, water-gas shift reaction and carbon formation via Boudouard reaction are included. The mechanism is implemented in a one-dimensional flow field description of a fixed bed reactor. The model is evaluated by comparison of numerical simulations with data derived from isothermal experiments in a flow reactor over a powdered nickel-based catalyst using varying inlet gas compositions and operating temperatures. Furthermore, the influence of hydrogen and water as co-feed on methane dry reforming with CO$_2$ is also investigated.

1. Introduction

In recent years, much attention has been paid towards the reforming of light hydrocarbons to produce synthesis gas (H_2/CO), which is an important intermediate in the chemical industry for manufacturing valuable basic chemicals and synthetic fuels, via methanol synthesis, oxo synthesis, and Fischer-Tropsch synthesis [1–6]. Hydrogen separated from the synthesis gas is largely used in the manufacturing of ammonia, a variety of petroleum hydrogenation processes, and for power generation [7–9]. Manufacturing syngas constitutes a significant portion of the investments in large-scale gas conversion plants based on natural gas [4].

Processes such as steam reforming (SR), partial oxidation (POX), autothermal reforming (ATR) and dry reforming (DR) are the most common catalytic technologies for converting natural gas to synthesis gas in various compositions [2].

Since 1930, the most important industrial method to produce syngas has been the steam reforming of methane Equation (1) [10,11]. Conventional steam reformers deliver relatively high concentrations of hydrogen at high fuel conversion [2,4,11,12]. The reaction is highly endothermic, and requires a large efficient external energy supply; also the efficiency of the process is severely affected by the catalyst deactivation due to carbon formation [4].

$$CH_4 + H_2O \rightarrow CO + 3H_2, \Delta H^0_{298} = 205.9 \frac{kJ}{mol} \tag{1}$$
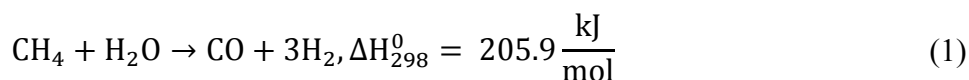
Due to the increasing environmental concerns about global warming and oil depletion, methane reforming with CO_2 Equation (2) has gained considerable attention in the field of catalysis, because it offers the opportunity to convert greenhouse gases (CH_4 and CO_2) as carbon-containing materials synthesis gas. The reforming of methane with CO_2 has been proposed for the production of H_2/CO with lower ratios, which is more suited for stream processes such as oxo synthesis of the aldehydes, syntheses of methanol, and acetic acid [13]. However, one of the main challenges in dry reforming of methane, especially at industrial conditions, is the formation of carbon, which causes catalyst deactivation [2,14].

$$CH_4 + CO_2 \rightarrow 2CO + 2H_2, \Delta H^0_{298} = 247.3 \frac{kJ}{mol} \tag{2}$$
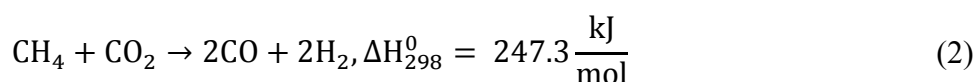
The catalytic partial oxidation Equation (3) of methane over nickel-based catalysts has been deeply studied as a promising alternative to the endothermic reforming processes [15–20], because no additional steam or heat are required. However, the process is complicated; different pre-treatment conditions affect the state of the catalyst surface and may change the reaction mechanism. Consequently, many studies have been carried out in order to elucidate the kinetics behind this reaction [15–21].

$$CH_4 + \frac{1}{2}O_2 \rightarrow CO + 2H_2, \Delta H^0_{298} = -36.0 \frac{kJ}{mol} \tag{3}$$
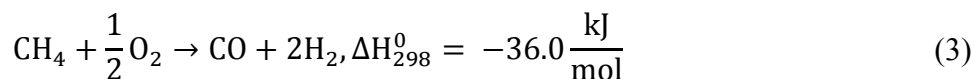
Similarly to the reforming processes, the catalytic oxidative conversion of methane at elevated temperatures and pressures suffers from coke formation as well. Coke deposition on catalysts and reactor pipe walls are serious problems in many industrial reactors that involve methane as fuel; in some cases it leads to the blocking of reactor tubes as well as the physical disintegration of the catalyst structure [22–27].

Noble metals have been found to be less prone to coke formation under oxidation and reforming conditions [28]. However, their high prices make them economically unsustainable. Ni-based catalysts are preferred in industrial applications due to fast turnover rates, good availability and low costs, but the use is limited by their higher tendency towards coke formation [29–31].

In order to optimize both the processes for the catalytic oxidation and reforming of methane, it is necessary to achieve a better understandings of the elementary steps involved in the reaction mechanism at a the molecular level and, along with the deactivation kinetics of coke formation. Here, micro-kinetic modeling is the approach of choice to cover different scales and varying conditions [32,33]. The kinetic model then needs to be is coupled with mass and heat transport models in order to numerically simulate the behavior of reforming reactors.

Reforming and oxidation of methane have been studied using several techniques. Different reaction mechanisms and corresponding kinetic models have been proposed. However, despite all reported experimental and theoretical studies, the detailed path for the conversion of methane to syngas and carbon remains a controversial issue [3]. In a pioneering work, Xu and Froment [11] proposed a reaction mechanism for the steam reforming of methane accompanied by water-gas shift reactions on a Ni/MgAl$_2$O$_4$ catalyst. Bradford and Vannice [13] studied the mechanism and kinetics of dry reforming over Ni catalysts with different supports. The authors proposed a model for CH$_4$-CO$_2$ kinetics based on CH$_4$ activation to form CH$_x$ and CH$_x$O. Aparicio [10] proposed an overall model that described CH$_4$-H$_2$O kinetics over Ni/MgO-MgAl$_2$O$_4$ catalysts. The rate constants of surface elementary reactions were extracted from transient isotopic experimental data by fitting the measured response curves to micro-kinetic models [10]. Chen *et al.* [31,32] modified Aparicio's micro-kinetic model for methane reforming with CO$_2$ and deactivation by carbon formation. Furthermore, they extended a hierarchical multiscale approach developed by Mhadeshwar and Vlachos [34] on Rh to a multiscale model of an industrial reformer for steam reforming on supported nickel catalysts. Wei and Iglesia [35] proposed a common sequence of elementary steps for CH$_4$ decomposition and water-gas shift reactions on Ni/MgO catalysts. Isotopic studies and reaction rate measurements showed a mechanistic equivalence among all CH$_4$ reactions [35]. Blaylock *et al*. [36,37] developed a micro-kinetic model for methane steam reforming using thermodynamic data from plane wave density functional theory (DFT) over nickel crystals. The model developed in this study predicts overall SR rates that are approximately 3 orders of magnitude slower than experimentally measured reforming rates using commercial supported catalysts. However, the comparison of calculated parameters with single-crystal Ni(111) high-resolution electron energy loss spectroscopy (HREELS) data shows the accuracy of the computational methods employed here at least for the case of methane decomposition. Wang *et al*. [38] investigated the reaction pathways of methane reforming with CO$_2$ on Ni (111) by using DFT calculations. The authors developed a surface reaction mechanism on the basis of computed energy barriers. There, the CH$_4$ dissociative adsorption is the rate determining step, and adsorbed CHO species are considered as key intermediates on the surface. The reaction paths for partial oxidation of methane and its kinetics over platinum and rhodium have been widely studied by several groups [34,39–43]. A review on catalytic partial oxidation of methane to synthesis gas with emphasis on reaction mechanisms over transition metal catalysts was published by Enger and co-workers [44]. De Groote and Froment [45] proposed a one-dimensional adiabatic model for partial oxidation of methane to syngas in a fixed bed reactor on nickel catalysts. The authors considered total and partial oxidation of methane, steam reforming, and water-gas shift.

Despite all the kinetic studies performed over nickel-based catalysts, the development of a detailed mechanism for simultaneous modeling of partial oxidation, steam and dry reforming of methane over nickel-based catalysts, as well as the sub systems behind these reactions (e.g., H_2 and CO oxidation, water-gas shift, and its reverse reaction) have not been described yet.

In this paper, we present an experimental and modeling study for catalytic conversion of methane under oxidative and reforming conditions over nickel-based catalysts. Therefore, in the present work a previously developed kinetic model for methane steam reforming over Ni/alumina catalysts [46] has been modified and extended. The newly developed thermodynamically consistent reaction mechanism includes carboxyl species (COOH) as an intermediate on the surface and new reaction paths for carbon formation. The mechanism is tested by the comparison of the simulation results with experimentally obtained data for partial oxidation, steam and dry reforming of methane over a powdered nickel-based catalyst in a temperature range of 373–1123 K.

2. Experimental Setup

Methane partial oxidation and reforming are studied in a fixed bed reactor as depicted in Figure 1. Details of the experimental setup can be found elsewhere [47]. The reactor consists of a quartz tube with an inner diameter of 10 mm filled with 20 mg of a nickel-based catalyst with a reaction zone of 27 mm length surrounded by a quartz frit and glass wool. The nickel-based catalyst was synthesized by BASF as part of the BMWI "DRYREF project" (reference FKZ0327856A) and has a particle size between 500 and 1000 μm.
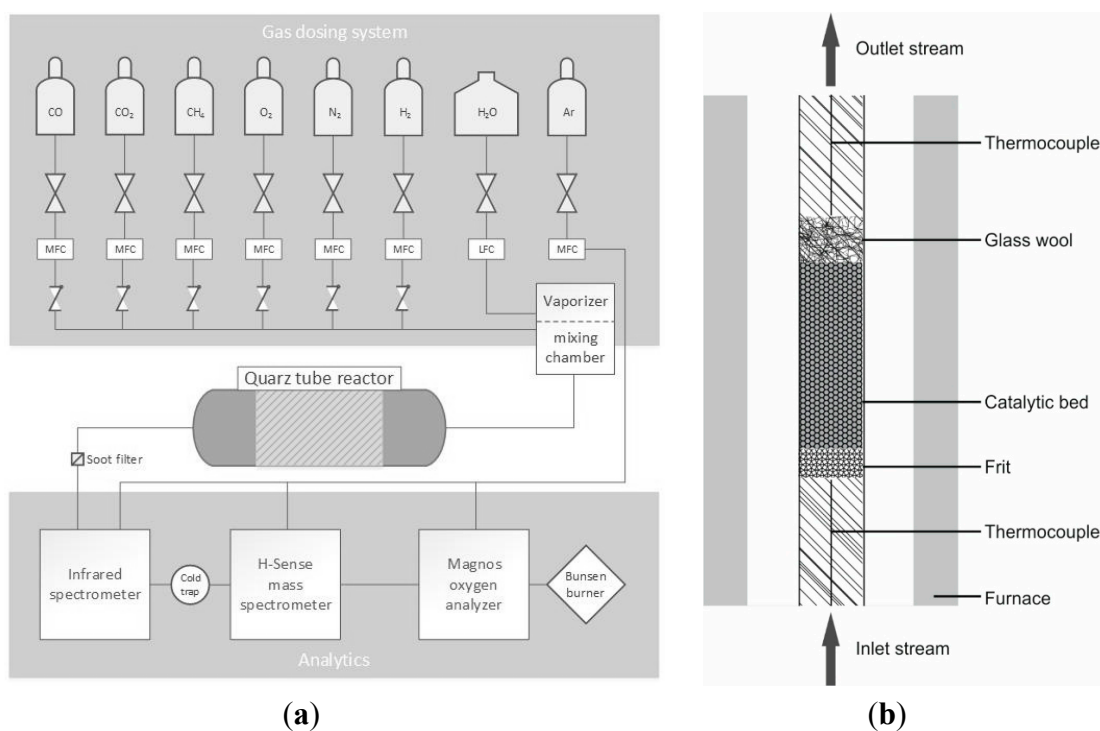
Figure 1. Schematic diagram of the experimental setup used for catalytic oxidation and reforming experiments over a nickel bed catalyst (**a**) and schematic drawing of the packed bed reactor (**b**).

The experiments were carried out at 4 slpm (standard liters per minute, T =298.15 K and p = 1.01325 bar) and 1 bar total pressure. The reaction temperatures were increased from 373 K to 1173 K at a rate of 15 K/min. Two separate thermocouples were used to measure the temperature of the gas-phase during the reaction: type K in front of the catalyst, and type N behind the catalyst, respectively. The entire reactor was surrounded by a furnace for heating and thermal insulation. Table 1 shows the different inlet compositions investigated in this study. The dosage of the gases (H_2, CO, O_2, CH_4, CO_2, and N_2) was controlled by mass flow controllers produced by Bronkhorst Hi-Tec. Water was provided by a liquid flow controller from a water reservoir. After evaporation, the water steam was mixed directly into the reactant gas stream.

Table 1. Investigated inlet gas mixtures on which the studies have been performed.

Fuel composition	CH_4 (vol.%)	O_2 (vol.%)	CO_2 (vol.%)	H_2 (vol.%)	H_2O (vol.%)	N_2 (vol.%)
CH_4/O_2	1.33	0.81	-	-	-	97.86
CH_4/H_2O	1.60	-	-	-	2.00	96.40
CH_4/CO_2	2.00	-	2.00	-	-	96.00
$CH_4/CO_2/H_2$	1.62	-	2.08	1.80	-	94.50
$CH_4/CO_2/H_2O$	1.67	-	2.13	-	2.13	94.07

The product composition was measured by means of an online Fourier Transform Infrared Spectrometer (FT-IR), a Mass spectrometer (H_2-MS) and paramagnetic oxygen detection (O_2-analyser, ABB, Zurich, Switzerland). Remaining water in the product stream was removed by a cold trap after passing the FT-IR to protect the downstream analytics. Argon was exclusively used as purifier gas for the analytics. Before all experiments, the powdered nickel-based catalyst was conditioned with 20 vol.% O_2 diluted in nitrogen at 673 K for 30 min and then reduced with 10 vol.% H_2 diluted in nitrogen with a total flow of 4 slpm at 873 K, over 60 min; then the reactor was cooled down to 373 K.

3. Mathematical Model and Numerical Simulation

The numerical simulation was performed using the software package DETCHEM™ [48], a program specifically designed for numerical simulation of the flow field coupled with detailed gas- phase and surface kinetics in chemical reactors at laboratory and technical scale.

All experiments used in the model development were carried out in a packed bed reactor at isothermal conditions.

3.1. Modeling the Flow Field in the Packed Bed Reactor

For simulations of the packed bed reactor the computer code DETCHEM[PACKEDBED] was used. The code uses an one-dimensional heterogeneous model that assumes no radial variations in the flow properties and axial diffusion of any quantity is negligible relative to the corresponding convective term [48].

The one-dimensional isothermal fixed-bed reactor model is based on the following set of equations:
Continuity equation

$$\frac{d(\rho u)}{dz} = a_v \sum_{i=1}^{N_g} \dot{s}_i M_i \tag{4}$$

Species conservation

$$\rho u \frac{d(Y_i)}{dz} + Y_i a_v \sum_{i=1}^{N_g} \dot{s}_i M_i = M_i(a_v \dot{s}_i + \dot{\omega}_i \varepsilon) \tag{5}$$

and equation of state

$$pM = \rho RT \tag{6}$$

Here, ρ = density, u = velocity, a_v = catalytic area to volume ratio, ε = porosity, A_c = area of cross section of the channel, N_g = number of gas-phase species, N_s = number of surface species, $\dot{s}_i$ = molar rate of production of species i by surface reaction, $\dot{\omega}_i$ = molar rate of production of species i by the gas-phase reaction, M_i = molecular mass of species i, Y_i = mass fraction of species , p = pressure, and M = average molecular weight. The porosity of the catalytic bed was calculated to be $\varepsilon = 0.42$, using a statistical method proposed by Pushnov [49]. The active catalytic area to volume ratio (a_v) was calculated by

$$a_v = D_{Ni} \cdot \frac{m_{Ni}}{M_{Ni}} \cdot \frac{1}{\Gamma} \cdot \frac{1}{V_{bed}} \tag{7}$$

The catalyst dispersion D_{Ni} was experimentally determined by chemisorption measurements. The surface-site density was chosen to be $\Gamma = 2.66 \times 10^{-5}\,\text{mol m}^{-2}$ [12,46]. In Equation (7), M_{Ni} represents the molar mass of nickel (58.7 g/mol), V_{bed} the total volume of the catalytic bed (m^3), and m_{Ni} the amount of catalyst loading (g). A value of $(a_v) = 9.85 \times 10^6\,\text{m}^{-1}$ was derived for the nickel-based catalyst used in this work.

3.2. Modeling the Surface Reaction Kinetics

The mean-field approximation is used to model the surface reaction kinetics. The approximation is related to the sizes of the computational cells in the flow field simulation, assuming that the local state of the active surface can be represented by means of values for this cell such as coverages (Θ_i) and temperature. [50,51]. A surface reaction is expressed as:

$$\sum_{i=1}^{N_g+N_s} v'_{ik} A_i \rightarrow \sum_{i=1}^{N_g+N_s} v''_{ik} A_i \tag{8}$$

where N_g is the number of gas-phase species, N_s is the number of surface species, with $v_{ik} = v''_{ik} - v'_{ik}$ are the stoichiometric coefficients and A_i denotes the species i. The concentration of the absorbed species can be expressed in terms of a surface coverage (Θ_i), according to the relation

$$\Theta_i = \frac{c_i \sigma_i}{\Gamma} \tag{9}$$

where c_i is the concentration of adsorbed species, which are given, e.g., in mol/m^2, σ_i represents the number of surface sites that are occupied by species i.

The total molar production rate $\dot{s}_i$ of surface species i on the catalyst was calculated in analogy to gas-phase reactions as a product of rate coefficients and concentrations determined by

$$\dot{s}_i = \sum_{k=1}^{K_s} v_{ik} \, k_{fk} \prod_{j=1}^{N_g+N_s} c_j^{v'_{jk}} \tag{10}$$

Thus, locally resolved reaction rates depend on the local gas-phase concentrations, surface coverage, and temperature.

The temperature dependence of the rate coefficients k_{fk} is described by a modified Arrhenius expression where additional coverage dependencies of the activation energy ε_{ik} are taken into account:

$$k_{fk} = A_k T^{\beta_k} \exp\left[\frac{-E_{ak}}{RT}\right] \prod_{i=1}^{N_s} \exp\left[\frac{\varepsilon_{ik} \Theta_i}{RT}\right] \tag{11}$$

Here, A_k is the pre-exponential factor, β_k the temperature exponent and E_{a_k} the activation energy. The rate for adsorption reactions were calculated using sticking coefficients $S_{o,i}$.

$$\dot{s}_i^{ads} = S_{o,i} \sqrt{\frac{RT}{2\pi M_i}} c_i \cdot \prod_{j=1}^{N_s} \Theta_j^{v'_j} \tag{12}$$

3.3. Sensitivity Analysis

Sensitivity analysis is used to identify the rate determining steps of the mechanism and their key parameters. In its simplest form we consider a perfectly mixed reactor at a constant temperature with only surface reactions. Then the change of amount n_i of species i is given by

$$\frac{dn_i}{dt} = A_{cat}\dot{s}_i \tag{13}$$

where A_{cat} is the catalytic surface area. We define a time dependent sensitivity coefficient $E_{i,k}(t)$ as the change of amount of species i with respect to a relative change of rate coefficient k_{fk}, *i.e.*,

$$E_{i,k}(t) = \frac{\partial n_i(t)}{\partial \ln k_{fk}}. \tag{14}$$

Inserting equations Equation (10) and Equation (13), we can solve for the time development of the sensitivity coefficient

$$\frac{dE_{i,k}(t)}{dt} = A_{cat} v_{ik} k_{fk} \prod_{j=1}^{N_g+N_s} c_j^{v'_{jk}} + A_{cat} \sum_{l=1}^{K_s} v_{il} \, k_{fl} \prod_{j=1}^{N_g+N_s} c_j^{v'_{jl}} \left(\sum_{j=1}^{N_g+N_s} v'_{jl} \frac{E_{j,l}}{n_j} \right) \tag{15}$$

Thus, the sensitivity coefficient describes the contribution of the kth reaction on the production of species i. Equation (15) can be integrated in time along with the solution of the conservation equations of each species. Since we are only interested in the relative contributions of all reactions on the products, we finally rescale the sensitivity coefficients for a given i such that the largest absolute value $|E_{i,k}|$ becomes unity.

3.4. Reaction Flow Analysis

Reaction flow analysis was used to identify the main pathway for the conversion of the reactants and the formation of the products. Here we look at individual contributions of a reaction k of the mechanism to the production or depletion of a chemical species i. The time-dependent production rate of species i by reaction k is

$$\frac{d\tilde{E}_{i,k}(t)}{dt} = \nu_{ik} k_{fk} \prod_{j=1}^{N_g+N_s} c_j^{\nu'_{jk}}$$

(16)

Only those $\tilde{E}_{i,k}$ for which species i is an immediate product of reaction k are of interest. Since all these $\tilde{E}_{i,k}$ are non-negative, they can be seen as weights in a directed graph that connects reactants and products along edges of elementary-step reactions. The $\tilde{E}_{i,k}$ are scaled such that the sum of the weights originating in a common root node becomes unity. Usually, only the most significant reactions are shown in the figures.

3.5. Thermodynamic Consistency

One of the requirements of a micro-kinetic model is that in the limit of infinite time the thermodynamic equilibrium is properly predicted. As a consequence, we need to guarantee that each elementary step is microkinetically reversible. Consider a pair of reversible reactions

$$\sum_{i=1}^{N_g+N_s} \nu'_{ik} \chi_i \overset{k_f}{\underset{k_r}{\rightleftarrows}} \sum_{i=1}^{N_g+N_s} \nu''_{ik} \chi_i \, .$$

(17)

For given temperature dependent rate coefficients $k_f(T)$ and $k_r(T)$, the equilibrium condition yields

$$\frac{k_f(T)}{k_r(T)} = K_c(T)$$

(18)

where $K_c(T)$ is the equilibrium constant with respect to concentrations. On the other hand, thermodynamic equilibrium is expressed by

$$K_p(T) = \exp\left(-\frac{\Delta_R G(T)}{RT}\right)$$

(19)

Here, $K_p(T)$ is the equilibrium constant with respect to pressures (or more precise: activities), $\Delta_R G(T)$ the change of Gibbs energy of the reaction, and R the universal gas constant. The two equilibrium constants can be converted by the factor

$$F_{c/p} = \frac{K_c(T)}{K_p(T)} = \prod_{i=1}^{N_g+N_s} \left(c_i^{\ominus}\right)^{\nu_i}$$

(20)

where $c_i^{\ominus}$ denotes the reference concentration of species i at standard pressure, *i.e.*, $c_i^{\ominus} = \frac{p^{\ominus}}{RT}$ for ideal gas species and $c_i^{\ominus} = \frac{\Gamma}{\sigma_i}$ for surface species. Thus, we can link the reaction rates to the thermodynamic properties by

$$\frac{k_f(T)}{k_r(T)} = F_{c/p} \cdot \exp\left(-\frac{\Delta_R G(T)}{RT}\right)$$ (21)

The change of Gibbs energy of a reaction can be written in terms of the Gibbs energies of each species.

$$\Delta_R G(T) = \sum_{i=1}^{N_g+N_s} v_i G_i(T) = \sum_{i=1}^{N_g+N_s} v_i\big(H_i(T) - T \cdot S_i(T)\big)$$ (22)

A reaction mechanism is considered thermodynamically consistent if Equation (21) is fulfilled for all reactions. The straight forward conclusion would be to use this equation to calculate the rate of the reverse reactions $k_r(T)$ for every forward rate $k_f(T)$. However, in the development of surface reaction mechanisms, the thermodynamic properties of surface species are often unknown. Therefore the rate coefficients for forward and reverse reactions need to be given explicitly. Nevertheless, thermodynamic consistency is satisfied for a reaction mechanism if a set of $G_i(T)$ for all surface species can be found such that Equation (21) is simultaneously satisfied for all pairs of reversible reactions.

A detailed surface reaction mechanism usually contains more pairs of reversible reactions than unknown thermodynamic functions $G_i(T)$. Thus, there are more equations of type Equation (21) than there are degrees of freedom to satisfy these equations (the latter is in most cases the number of surface species minus one). So, $k_f(T)$ and $k_r(T)$ cannot be chosen independently for all reactions.

In a previous publication [46] we described a method to ensure thermodynamic consistency in such a case. There, no assumptions about the functions $G_i(T)$ were made, just their existence was required. However, it turned out that by doing so, the adjusted mechanisms may have required some species with negative heat capacity. Obviously such a mechanism cannot be claimed to be realistic in detail. Therefore, the algorithm has been improved by considering physically meaningful temperature dependencies of the functions $G_i(T)$. We will only limit to the case of constant heat capacities c_{pi} for surface species. Then the enthalpy must be a linear function of temperature

$$H_i(T) = H_{0i} + c_{pi} \cdot (T - T_0)$$ (23)

and the entropy contains a logarithmic dependency

$$S_i(T) = S_{0i} + c_{pi} \cdot \ln\left(\frac{T}{T_0}\right)$$ (24)

Thus, the Gibbs energy becomes

$$G_i(T) = H_{0i} + c_{pi} \cdot (T - T_0) - TS_{0i} + c_{pi}T \cdot \ln\left(\frac{T}{T_0}\right)$$ (25)

Taking the logarithm of Equation (21) and separating the known (*i.e.*, for gas-phase species) and the unknown (*i.e.*, for surface species) thermodynamic variables, we get

$$\ln k_f - \ln k_r = \ln F_{c/p} - \sum_{i=1}^{N_g} v_i \frac{G_i(T)}{RT}$$
$$- \sum_{i=N_g+1}^{N_g+N_s} \frac{v_i}{R}\left[\frac{H_{0i} - c_{pi}T_0}{T} + c_{pi}(1 - \ln T_0) - S_{0i} + c_{pi}\ln T\right]$$ (26)

The temperature dependent term of the rate coefficients is given according to Equation (11) by

$$k_{f,r}(T) = A_{f,r} \cdot T^{\beta_{f,r}} \cdot \exp\left(-\frac{E_{af,r}}{RT}\right) \tag{27}$$

Adsorption reactions can be treated in the same way by converting expressions based on sticking coefficients into the same functional form.

Obviously the terms $\ln k_f$, $\ln k_r$ and $\frac{G_i(T)}{RT}$ for the surface species with unknown thermodynamic properties belong to a set of functions

$$\boldsymbol{F} = \left\{ y(T) = a + b \ln T + \frac{c}{T} \,\middle|\, a, b, c \in \mathbb{R} \right\} \tag{28}$$

with constant coefficients a , b and c . The objective to make a reaction mechanism thermodynamically consistent is now to find functions $x_k(T) \in \boldsymbol{F}$ and $y_i(T) \in \boldsymbol{F}$ such that

$$(\ln k_f + x_f(T)) - (\ln k_r - x_r(T)) = \ln F_{c/p} - \sum_{i=1}^{N_g} v_i \frac{G_i(T)}{RT} - \sum_{i=N_g+1}^{N_g+N_s} v_i \cdot y_i(T) \tag{29}$$

is fulfilled for all reactions. Here $x_k(T)$ shall denote the necessary changes in the rate coefficients of a proposed reaction mechanism. With good agreement over a wide temperature range, we can approximate the given terms by a function $z(T) \in \boldsymbol{F}$

$$z(T) = \ln F_{c/p} - \sum_{i=1}^{N_g} v_i \frac{G_i(T)}{RT} - \ln k_f + \ln k_r \tag{30}$$

Therefore, the problem is transformed to solve a system of equations for pairs of reversible reactions k:

$$x_{fk}(T) - x_{rk}(T) = z_k(T) - \sum_{i=N_g+1}^{N_g+N_s} v_{ik} \cdot y_i(T) \tag{31}$$

It is not necessary to correct all reactions with terms $x_k(T)$. Some of these terms may be omitted, which means that the rate coefficients shall not be changed in the adjustment. The method proposed by Mhadeshvar and Vlachos [52], for instance, keeps a maximum number of reactions unchanged and adjusts exactly one reaction for each so-called thermodynamic cycle. In our iterative reaction mechanism development process, we fix the parameters of reactions that were identified to be most sensitive, leaving an underdetermined system of linear Equation (31).

For this underdetermined system of equations we are interested in the solution that minimizes the necessary changes to the effective rate constants in terms of an objective function

$$\Phi = \sum_k w_k \cdot \|x_k\|^2 \rightarrow \min \tag{32}$$

where w_k are selectable non-negative weights and

$$\|x_k\|^2 = \int_{T_1}^{T_2} (x_k(T))^2 \, dT \tag{33}$$

We can use the method of Lagrange multipliers to minimize the objective function Φ. As result we get correction terms $x_k(T)$ and thermodynamic functions $y_i(T)$.

This algorithm can also easily be extended to coverage dependent rate expressions as in Equation (11) by formulation of the minimization problem for each species i with non-zero coverage dependent activation energies ϵ_{ik} by assuming coverage-dependent Gibbs Free Energies

$$G_i(T) = H_{0i} + c_{pi} \cdot (T - T_0) - TS_{0i} + c_{pi}T \cdot \ln\left(\frac{T}{T_0}\right) + \sum_j \epsilon_{ij}\Theta_j \qquad (34)$$

Finally, the adjustment algorithm yields a surface reaction mechanism with minimum changes in the Arrhenius rate constants and coverage dependent activation energies. The resulting mechanism is thermodynamically consistent in the sense that thermodynamic functions with correct temperature dependency exist for all species. This procedure needs to be applied during mechanism development every time a rate coefficient has been changed manually.

4. Surface Reaction Mechanism

The conversion of methane to syngas includes different molecular paths considered as a combination of the following overall reactions (Table 2).

Table 2. Overall reactions (OR_x) in the methane reforming and oxidation system.

OR_x	Reaction	Reaction Enthalpy
	Methane Steam Reforming	
OR_1	$CH_4 + H_2O \leftrightarrow CO + 3H_2$	$\Delta H^\circ_{298} = 205.9$ kJ/mol
OR_2	$CH_4 + 2H_2O \leftrightarrow CO_2 + 4H_2$	$\Delta H^\circ_{298} = 164.7$ kJ/mol
	Methane dry reforming	
OR_3	$CH_4 + CO_2 \leftrightarrow 2CO + 2H_2$	$\Delta H^\circ_{298} = 247.3$ kJ/mol
	Methane partial oxidation	
OR_4	$CH_4 + 1/2O_2 \leftrightarrow CO + 2H_2$	$\Delta H^\circ_{298} = -35.6$ kJ/mol
	Methane total oxidation	
OR_5	$CH_4 + 2O_2 \leftrightarrow CO_2 + 2H_2O$	$\Delta H^\circ_{298} = -880$ kJ/mol
	Water-gas shift	
OR_6	$CO + H_2O \leftrightarrow CO_2 + H_2$	$\Delta H^\circ_{298} = -41.2$ kJ/mol
	Methanation	
OR_7	$CO + 3H_2 \leftrightarrow CH_4 + H_2O$	$\Delta H^\circ_{298} = -206$ kJ/mol
OR_8	$2CO + 2H_2 \leftrightarrow CH_4 + CO_2$	$\Delta H^\circ_{298} = -247$ kJ/mol
	Boudouard reaction	
OR_9	$2CO \leftrightarrow^* C + CO_2$	$\Delta H^\circ_{298} = -172.4$ kJ/mol
	Methane cracking	
OR_{10}	$CH_4 \leftrightarrow^* C + 2H_2$	$\Delta H^\circ_{298} = 74.9$ kJ/mol
	Gasification of carbon	
OR_{11}	$^* C + H_2O \leftrightarrow CO + H_2$	$\Delta H^\circ_{298} = 131.3$ kJ/mol
OR_{12}	$^* C + O_2 \leftrightarrow CO_2$	$\Delta H^\circ_{298} = -393.5$ kJ/mol

* C as graphite.

A previously established model for steam reforming on nickel [46] served as basis for the development of a kinetic scheme for the extended region of operating conditions covering all the ways from total oxidation to pyrolysis. The unity bond index-quadratic exponential potential (UBI-QEP) approach [53–55] was applied to determine heats of adsorption of adsorbed species, reaction enthalpy changes, and the original activation barriers for all relevant steps of the mechanism. Here, the reaction scheme is extended by adding new reaction paths involving carboxyl species as intermediate together with carbon formation paths.

The thermodynamically consistent surface reaction mechanism presented in Table 3 was developed using several sets of experiments for oxidation and reforming of methane. The predictive behavior of the overall reactor model was assessed by adaption of the kinetics through iterative comparisons of numerically predicted and experimentally determined species concentrations. The new model consists of 52 reactions with 6 gas-phase species and 14 surface species.

The kinetic model presented in Table 3 involves adsorption and desorption steps of all reactants and products, as well as surface reaction steps. Figure 2 describes the main pathways for methane reforming and oxidation processes on the nickel catalyst for syngas production. The availability of adsorbed atomic oxygen O(s), produced via dissociative adsorption of O_2, H_2O or CO_2, plays an important role to determine the reaction rate of these reactions. The importance of this common reaction intermediate is supported by TPR experimental results obtained by Qin *et al.* [56], *in situ* isotope transient experiments performed by Aparicio [10], and DFT studies carried out by Zu *et al.* [14]. Sticking coefficients were used to model adsorption reactions (H_2, CH_4, CO, CO_2, O_2, and H_2O). The initial values of the sticking coefficients were taken from the previous kinetic model [46].

The initial kinetic data are based on the surface science literature, which will be summarized below for individual steps.

4.1. H_2 on Ni Surface

Hydrogen desorption from nickel was studied by many authors, the activation energy was found to be between 90 and 97 kJ/mol for a single crystal surface. Bartholomew [57] and Weatherbee [58] reported heats of adsorption in a range of approximately 82–89 kJ/mol. Katzer *et al.* [59] calculate a H_2 desorption energy of 96 kJ/mol. Chen *et al.* [32] estimated the activation energy for H_2 desorption to be 97 kJ/mol applying the UBI-QEP method; this value is close to the parameter obtained by Zhu and White [60], using static secondary ion mass spectroscopy (SSIMS) on Ni(100) of 95 kJ/mol and the activation energy of 96 kJ/mol reported by Aparicio [10]. Bengaard *et al.* [61] determined the activation energies of desorption of H_2 from Ni(111), Ni(100), Ni(110) and Ni(445) to be 96, 90, 89, and 87 kJ/mol, respectively.

The activation energy for hydrogen desorption of 81.21 kJ/mol used in our previous model was estimated by the UBI-QEP method. However, this value was too low in comparison with the results reported by the previous mentioned references using different theoretical and experimental methods. In the new model, the activation energy for hydrogen desorption was modified from 81.21 kJ/mol to 95 kJ/mol, nevertheless the model predicts former and the currently presented experimental data. This modification shows an improvement in the prediction for hydrogen production via water-gas shift reaction (WGS), especially at high temperatures.

Table 3. Surface reaction mechanism for methane oxidation and reforming over Ni-based catalyst.

Rx	Reaction	$A/(\text{cm}^2/\text{mol·s})/S_0$	β	$E_a/(\text{kJ/mol})$	ε_l (kJ/mol)
R1	$H_2 + Ni(s) + Ni(s) \rightarrow H(s) + H(s)$	3.00×10^{-2}	0.000	5.0	
R2	$H(s) + H(s) \rightarrow Ni(s) + Ni(s) + H_2$	$2.54 \times 10^{+20}$	0.000	95.2	
R3	$O_2 + Ni(s) + Ni(s) \rightarrow O(s) + O(s)$	4.36×10^{-2}	−0.206	1.5	
R4	$O(s) + O(s) \rightarrow Ni(s) + Ni(s) + O_2$	$1.18 \times 10^{+21}$	0.823	468.9	
R5	$H_2O + Ni(s) \rightarrow H_2O(s)$	1.00×10^{-1}	0.000	0.0	
R6	$H_2O(s) \rightarrow H_2O + Ni(s)$	$3.73 \times 10^{+12}$	0.000	60.7	
R7	$CO_2 + Ni(s) \rightarrow CO_2(s)$	7.00×10^{-6}	0.000	0.0	
R8	$CO_2(s) \rightarrow CO_2 + Ni(s)$	$6.44 \times 10^{+7}$	0.000	25.9	
R9	$CO + Ni(s) \rightarrow CO(s)$	5.00×10^{-1}	0.000	0.0	
R10	$CO(s) \rightarrow CO + Ni(s)$	$3.56 \times 10^{+11}$	0.000	111.2	$-50.0\ \theta_{CO(s)}$
R11	$CH_4 + Ni(s) \rightarrow CH_4(s)$	8.00×10^{-3}	0.000	0.0	
R12	$CH_4(s) \rightarrow CH_4 + Ni(s)$	$8.70 \times 10^{+15}$	0.000	37.5	
R13	$CH_4(s) + Ni(s) \rightarrow CH_3(s) + H(s)$	$1.54 \times 10^{+21}$	0.087	55.8	
R14	$CH_3(s) + H(s) \rightarrow CH_4(s) + Ni(s)$	$1.44 \times 10^{+22}$	−0.087	63.4	
R15	$CH_3(s) + Ni(s) \rightarrow CH_2(s) + H(s)$	$1.54 \times 10^{+24}$	0.087	98.1	
R16	$CH_2(s) + H(s) \rightarrow CH_3(s) + Ni(s)$	$3.09 \times 10^{+23}$	−0.087	57.2	
R17	$CH_2(s) + Ni(s) \rightarrow CH(s) + H(s)$	$3.70 \times 10^{+24}$	0.087	95.2	
R18	$CH(s) + H(s) \rightarrow CH_2(s) + Ni(s)$	$9.77 \times 10^{+24}$	−0.087	81.0	
R19	$CH(s) + Ni(s) \rightarrow C(s) + H(s)$	$9.88 \times 10^{+20}$	0.500	21.9	
R20	$C(s) + H(s) \rightarrow CH(s) + Ni(s)$	$1.70 \times 10^{+24}$	−0.500	157.9	
R21	$CH_4(s) + O(s) \rightarrow CH_3(s) + OH(s)$	$5.62 \times 10^{+24}$	−0.101	92.7	
R22	$CH_3(s) + OH(s) \rightarrow CH_4(s) + O(s)$	$2.98 \times 10^{+22}$	0.101	25.8	
R23	$CH_3(s) + O(s) \rightarrow CH_2(s) + OH(s)$	$1.22 \times 10^{+25}$	−0.101	134.6	
R24	$CH_2(s) + OH(s) \rightarrow CH_3(s) + O(s)$	$1.39 \times 10^{+21}$	0.101	19.0	
R25	$CH_2(s) + O(s) \rightarrow CH(s) + OH(s)$	$1.22 \times 10^{+25}$	−0.101	131.3	
R26	$CH(s) + OH(s) \rightarrow CH_2(s) + O(s)$	$4.40 \times 10^{+22}$	0.101	42.4	
R27	$CH(s) + O(s) \rightarrow C(s) + OH(s)$	$2.47 \times 10^{+21}$	0.312	57.7	
R28	$C(s) + OH(s) \rightarrow CH(s) + O(s)$	$2.43 \times 10^{+21}$	−0.312	118.9	
R29	$H_2O(s) + Ni(s) \rightarrow H(s) + OH(s)$	$3.67 \times 10^{+21}$	−0.086	92.9	
R30	$H(s) + OH(s) \rightarrow H_2O(s) + Ni(s)$	$1.85 \times 10^{+20}$	0.086	41.5	
R31	$H(s) + O(s) \rightarrow OH(s) + Ni(s)$	$3.95 \times 10^{+23}$	−0.188	104.3	
R32	$OH(s) + Ni(s) \rightarrow H(s) + O(s)$	$2.25 \times 10^{+20}$	0.188	29.6	
R33	$OH(s) + OH(s) \rightarrow H_2O(s) + O(s)$	$2.34 \times 10^{+20}$	0.274	92.3	
R34	$H_2O(s) + O(s) \rightarrow OH(s) + OH(s)$	$8.14 \times 10^{+24}$	−0.274	218.4	
R35	$C(s) + O(s) \rightarrow CO(s) + Ni(s)$	$3.40 \times 10^{+23}$	0.000	148.1	
R36	$CO(s) + Ni(s) \rightarrow C(s) + O(s)$	$1.75 \times 10^{+13}$	0.000	116.2	
R37	$CO(s) + H(s) \rightarrow C(s) + OH(s)$	$3.52 \times 10^{+18}$	−0.188	105.4	
R38	$C(s) + OH(s) \rightarrow H(s) + CO(s)$	$3.88 \times 10^{+25}$	0.188	62.5	$-50.0\ \theta_{CO(s)}$
R39	$CO(s) + CO(s) \rightarrow C(s) + CO_2(s)$	$1.62 \times 10^{+14}$	0.500	241.7	$-50.0\ \theta_{CO(s)}$

Table 3. *Cont.*

Rx	Reaction	$A/(\text{cm}^2/\text{mol·s})/S_0$	β	$E_a/(\text{kJ/mol})$	ε_1 (kJ/mol)
R40	$CO_2(s) + C(s) \rightarrow CO(s) + CO(s)$	$7.29 \times 10^{+28}$	−0.500	239.2	$-100.0\ \theta_{CO(s)}$
R41	$CO(s) + O(s) \rightarrow CO_2(s) + Ni(s)$	$2.00 \times 10^{+19}$	0.000	123.6	
R42	$CO_2(s) + Ni(s) \rightarrow CO(s) + O(s)$	$4.64 \times 10^{+23}$	−1.000	89.3	$-50.0\ \theta_{CO(s)}$
R43	$CO(s) + OH(s) \rightarrow COOH(s) + Ni(s)$	$6.00 \times 10^{+21}$	0.213	97.6	
R44	$COOH(s) + Ni(s) \rightarrow CO(s) + OH(s)$	$1.46 \times 10^{+24}$	−0.213	54.3	
R45	$CO_2(s) + H(s) \rightarrow COOH(s) + Ni(s)$	$6.25 \times 10^{+24}$	−0.475	117.2	
R46	$COOH(s) + Ni(s) \rightarrow CO_2(s) + H(s)$	$3.73 \times 10^{+20}$	0.475	33.6	
R47	$CO(s) + H(s) \rightarrow HCO(s) + Ni(s)$	$4.00 \times 10^{+20}$	−1.000	132.2	$-50.0\ \theta_{CO(s)}$
R48	$HCO(s) + Ni(s) \rightarrow CO(s) + H(s)$	$3.71 \times 10^{+21}$	0.000	0.0	
R49	$HCO(s) + Ni(s) \rightarrow CH(s) + O(s)$	$3.79 \times 10^{+14}$	0.000	81.9	$+50.00\theta_{CO(s)}$
R50	$CH(s) + O(s) \rightarrow HCO(s) + Ni(s)$	$4.59 \times 10^{+20}$	0.000	109.9	
R51	$H(s) + COOH(s) \rightarrow HCO(s) + OH(s)$	$6.00 \times 10^{+22}$	−1.163	104.8	
R52	$HCO(s) + OH(s) \rightarrow COOH(s) + H(s)$	$2.28 \times 10^{+20}$	0.263	15.9	

The rate coefficients are given in the form of $k = AT^{\beta} \exp(-E_a/RT)$; adsorption kinetics is given in form of sticking coefficients; the surface site density is $\Gamma = 2.66 \times 10^{-9}$ mol·cm^{-2} [12,46]. Rx represents the reaction number.
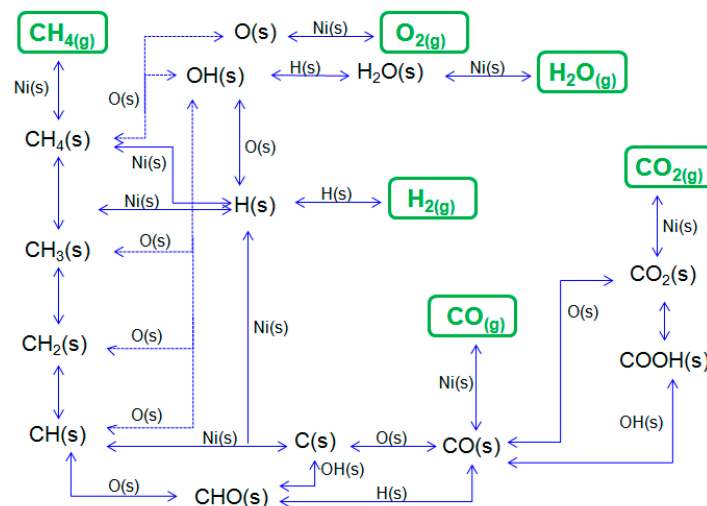

Figure 2. Reaction pathways for methane oxidation and reforming.

4.2. O_2 on Ni Surface

The interaction of oxygen with nickel was subject of a large number of surface science studies using a wide range of techniques. Stuckless *et al.* [62] listed the initial heats of adsorption of oxygen for the three low index crystal planes of Ni. The activation energies for desorption are 520 kJ/mol, 470 kJ/mol, and 485 kJ/mol for the Ni(100), Ni(111) and Ni(110) planes, respectively. These values are similar to the *ab-initio* theoretical results obtained by Siegbahn and Wahlgren [63]; in their work 540 kJ/mol was estimated for Ni(100) and 480 kJ/mol for Ni(111). In our model, the activation energy for oxygen desorption R4 of 468.9 kJ/mol was estimated by UBI-QEP method; being close to the activation energy for Ni(111) proposed by Stuckless *et al.* [62].

4.3. H_2O on Ni Surface

The desorption of H_2O has been studied by Stulen *et al.* [64] at a low temperature on clean Ni(111) using thermal desorption spectrometry (TDS) and electron-simulated desorption (ESD). They reported an activation energy for H_2O desorption of 41 kJ/mol. Pache *et al.* [65] reported an activation energy for H_2O desorption of 57 ± 5 kJ/mol measured for a clean Ni(111) surface. Chen *et al.* [31] considered desorption energies for H_2O of 64.4 kJ/mol in their macro-kinetic model. Aparicio [10] performed detailed micro-kinetic studies of the hydrogen exchange reaction of H_2O with D_2 on Ni/MgAl$_2$O$_3$ and reports an activation energy of 64.4 kJ/mol for H_2O desorption. Zakharov *et al.* [66] performed theoretical cluster calculations on Ni(111); leading to activation energies between 51.4 kJ/mol and 67.1 kJ/mol. The value of 60.8 kJ/mol used in the present work for H_2O desorption is comparable with the experimental and theoretical values reported in the literature.

4.4. CO on Ni Surface

Estimated values for CO desorption found in theoretical studies using DFT calculations are in the range of 120 ± 10 kJ/mol [32,36,67,68]. Using temperature-programmed desorption (TPD) Bjørgum *et al.* [69] derived a CO desorption energy of 119 kJ/mol for low CO surface coverages. Al-Sarraf *et al.* [70] estimated an initial heat of CO adsorption of 122 ± 4 kJ/mol for Ni(100) using a single crystal micro-calorimeter. In our work, the heat of CO adsorption of 111.27 kJ/mol was estimated from the UBI-QEP method and is close to the value of 115 kJ/mol as reported by Aparicio [10]. Coverage dependency for CO is included into the kinetic model to describe the lateral interaction of adsorbed species. The values were estimated based on the comparison of model predictions and experimental results.

4.5. CH_4 on Ni Surface

The reference values for the activation energies of methane dehydrogenation (R11–R19), oxygen assisted methane dehydrogenation (R21–R27), water activation (R29–R34), and CO dissociation (R35–R36) are taken from our former kinetic study for steam reforming on nickel [46]; such values were slightly modified due to the computational algorithm that is applied to guarantee thermodynamic consistency [71].

4.6. C on the Ni Surface

The surface reaction mechanism includes reaction paths to describe the formation of up to one monolyer of carbon from adsorbed CO species. The first path is through CO(s) dissociation (R35–R36); the reference values for activation barriers of this reaction are taken from our former mechanism [46]. In the current mechanism, we introduce new reaction paths for carbon formation (R37–R40). The reaction steps R37–R38 were estimated by the UBI-QEP method. The Boudouard reaction (R39–R40) is also included in the model; the activation energies of these reactions are based on the kinetic data reported by Blaylock *et al.* [37] from DFT calculations. However, such data were modified within the enthalphic consistency.

4.7. COOH on Ni Surface

Two reaction paths are proposed for CO oxidation. The first path is the direct oxidation of CO(s) with O(s) (R41–R42). The second one takes place through the surface intermediate carboxyl (COOH) formed from CO(s) and OH(s). It is assumed that COOH(s) binds to the surface by its carbon atom. Formate (HCOO) as additional reactive surface intermediate has been discussed in the literature [72–74]; it is bonded to the surface through its oxygen atom. Carboxyl and formate intermediates are isomers and both have been detected experimentally over different transition metals [73,75–79]. Tibiletti *et al.* [78] identified formate, carbonate and carboxyl species at the surface of a Pt/CeO_2 catalyst during the forward water-gas shift (WGS) and the reverse reaction (RWGS). Shido and Iwasawa [79] also studied the formation of formate species on Rh/CeO_2 during WGS. Despite all studies performed, there is still no overall agreement on the nature of the rate-determining intermediate, as to whether it is a carboxyl or a formate species. Theoretical calculations favor the formation of carboxyl species, while the surface formate is considered as a spectator species [80,81]. Lin *et al.* [82] performed mechanistic studies using density functional theory (DFT) to clarify the mechanism of WGS reaction on transition metals. The authors proposed that the WGS reaction involves three mechanisms: (i) redox; (ii) carboxyl; and (iii) formate. Lin *et al.* [82] showed that the formate path is energetically unfavorable in comparison to the redox and carboxyl mechanisms. The carboxyl mechanism is supported by Boisen *et al.* [83], who assumed that the carboxyl species plays an important role especially on supports containing CeO_2, regardless of the metal type, that the extraction of the first hydrogen from water is a slow step and that the subsequent reaction of CO and OH results in a carboxyl (COOH) intermediate which decomposes into CO_2 and H_2. Grabow *et al.* [84] presented a micro-kinetic model as well as experimental data for the low-temperature water-gas shift (WGS) reaction catalyzed by Pt at temperatures ranging from 523 K to 573 K for various gas compositions at a pressure of 1 atm. The authors concluded that the most significant reaction channel proceeds via the carboxyl (COOH) intermediate. Gokhale *et al.* [80] used self-consistent density functional theory (DFT-GGA) calculations to investigate the WGS mechanism on Cu(111) and identified carboxyl, as central intermediate. In a recent study, Karakaya *et al.* [85] developed a kinetic model for the WGS reaction over Rh. In this model, the main path for CO_2 formation is concluded to be the direct oxidation of CO with O species at high temperatures, whereas the formation of the carboxyl group is significant at low temperatures.

During the development of our kinetic model, sensitivity and reaction flow analysis were performed to determine the significance of both reactions paths. The analysis showed that the carboxyl path was more sensitive especially for conditions were water was added as co-feed. However, the results did not show a significant participation of the formate intermediate in any of the cases studied. Therefore, we do not further consider the formate path in the reaction mechanism. The DFT calculation data presented by Blaylock *et al.*[36,37] for steam reforming on nickel are used as a reference for the reaction paths and enthalpy values in (R43–R46) (Table 3).

4.8. HCO on Ni surface

It has been proposed by several authors that formyl species (HCO) are coordinated through carbon and acts as intermediate during the reforming and oxidation of methane over transition metals [31,32,37,38,86,87].

Pistonesi *et al.* [88] have studied HCO(s) on Ni(111) and proposed based on DFT calculations that during methane steam reforming on nickel, dissociation of HCO(s) to CO(s) and H(s) is favored. Zhou *et al.* [14] concluded from their DFT studies that HCO is a key intermediate during dry reforming of methane to CO and H_2. Blaylock *et al.* [36] studied the kinetics of steam reforming over Ni(111). Based on DFT calculations they obtain an activation energy of 150 kJ/mol for the $CH(s) + O(s) \rightarrow HCO(s)$ step. The authors also conclude that the formation of HCO(s) is an important step during steam reforming of methane. Chen *et al.* [32] also includes the HCO(s) surface species as intermediate in their micro-kinetic model for methane reforming.

The implementation of the HCO(s) in the kinetic model presented in this work is supported experimentally by TPRS and TR-FTIR experiments [89] and theoretically by the UBI-QEP method [54,90] as well as DFT studies [36–38]. Our previous mechanism [46] is used as a reference for the kinetic data for the reaction steps R47 and R50, where HCO(s) is produced from CO(s) and from CH(s). In addition to these reactions, the formation of HCO(s) through carboxyl intermediate (R51–R52) is also included. The kinetic data presented by Chen *et al.* [32] are used as a reference for R51–R52 in our model.

5. Results and Discussion

5.1. Methane Catalytic Partial Oxidation (CPOX)

Catalytic partial oxidation of methane has been extensively studied [5,15–20,39–44,91–94]. Nevertheless, the mechanism of syngas production is still controversial. Two main paths have been suggested for partial oxidation of methane. On the one hand, the direct oxidation mechanisms where H_2 is directly originated from methane decomposition. Further interaction of adsorbed hydrocarbon species CH_x ($x = 0, 1, 2, 3$) with adsorbed atomic oxygen produces carbon monoxide [5,42,91,94,95]. On the other hand, the indirect route where methane is totally oxidized to CO_2 and H_2O, as long as oxygen is present close to the catalyst surface, and then the remaining CH_4 is reformed with steam or CO_2 to H_2 and CO [15,39,41,43,96–98].

Figure 3 shows the experimentally measured species concentrations in comparison with the numerical predictions as a function of the temperature in our fixed bed reactor. Methane conversion starts at 723 K leading to CO_2 and H_2O formation only. No significant amounts of H_2 or CO were detected up to a temperature of 880 K. At temperatures above 880 K, H_2 and CO formation increases while, CO_2 and H_2O concentrations decrease leading almost to the equilibrium composition at given operating conditions (Figure 3b).

CO_2 and H_2O concentrations are above the ones obtained at equilibrium in the medium temperature range. At equilibrium more H_2 and CO is predicted. This behavior is an indication for the indirect way to H_2 and CO via formation of H_2O and CO_2.
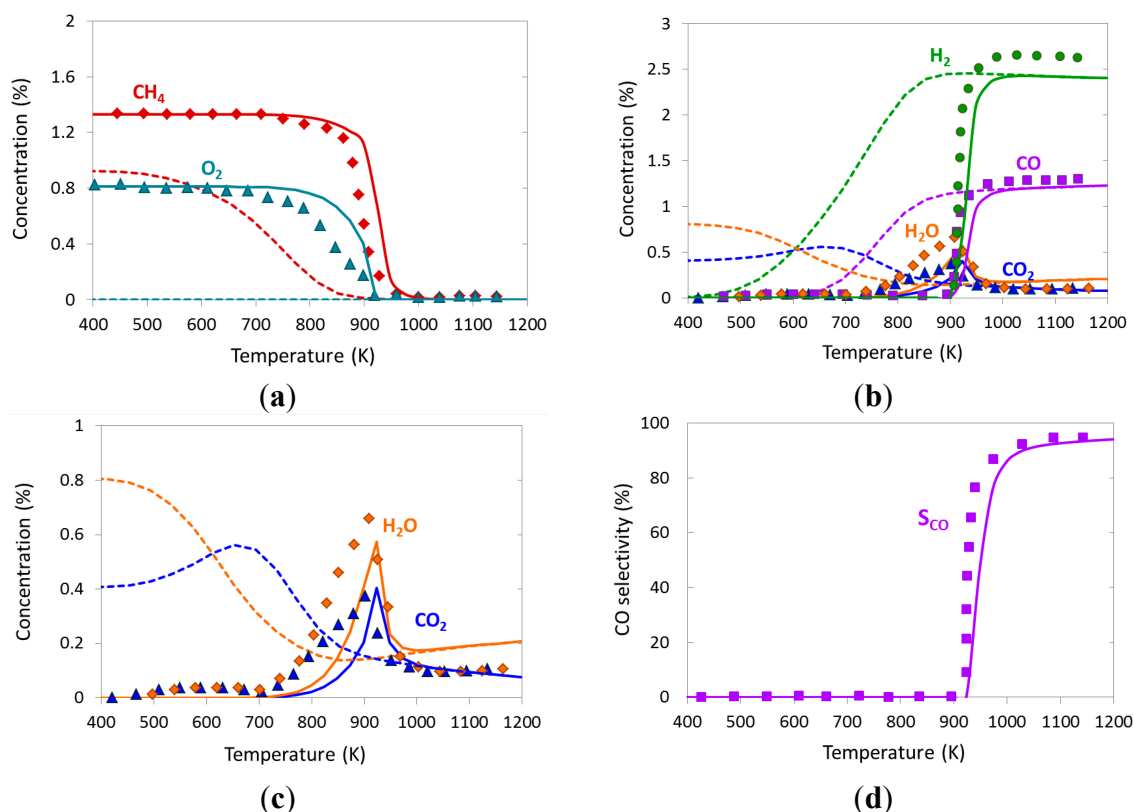
Figure 3. Comparison of experimentally determined (symbols) and numerically predicted (lines) concentrations as a function of temperature for catalytic partial oxidation of methane in a fixed bed reactor: (**a**) reactants; (**b**) products; (**c**) zoom-in of CO_2 and H_2O formation; (**d**) selectivity of CO; inlet gas composition of $CH_4/O_2 = 1.6$ in N_2; 1 bar; $T_{inlet} = 373$ K; total flow rate of 4 slpm; dashed lines = equilibrium composition at given temperature.

Numerically predicted concentrations of O_2 and CH_4 (Figure 3a) as well as H_2 and CO (Figure 3b) concentrations agree well with the experimentally derived data in the whole temperature range under investigation. The selectivity of CO is presented in Figure 3d.

The computed concentrations of the gas-phase species along the catalytic bed at 973 K after ignition (Figure 4) also support the indirect route of H_2 and CO formation. At the beginning of the catalytic bed CO_2 and H_2O are first formed by total oxidation of methane, whereas H_2 and CO are produced through steam and some dry reforming of methane further downstream when oxygen is completely consumed. The very distinct transition for total oxidation and reforming at an axial position of 14 mm is also caused by the fact that a one-dimensional packed-bed model is used, *i.e.*, mass transfer limitations are neglected.

There is a competitive adsorption between CH_4 and O_2 species on metallic nickel sites during partial oxidation of methane. However, O_2 adsorption is stronger than that of CH_4 [21]. Before ignition, the surface is mainly covered by oxygen; the system is controlled by surface reaction kinetics. Figure 5 shows the computed surface coverage at 973 K after ignition. Oxygen coverage is dominating the entrance region of the catalytic bed where oxygen is available in the gas flow. At an axial position of 14 mm, the oxygen coverage decreases fast, producing free nickel sites together with carbon monoxide and adsorbed hydrogen. The species OH(s) and H_2O(s) have a maximum concentration on the surface at the transition point (Figure 5b). Further downstream some carbon C(s) increases on the surface.
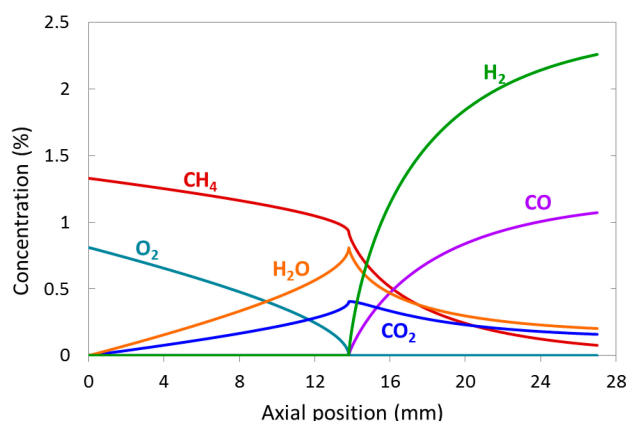
Figure 4. Computed concentration of the gas-phase species: O_2, CH_4, H_2, H_2O, CO and CO_2 along the catalytic bed after the ignition for partial oxidation of methane over nickel at 973 K, $CH_4/O_2 = 1.6$ and 1 bar.

(a)   (b)
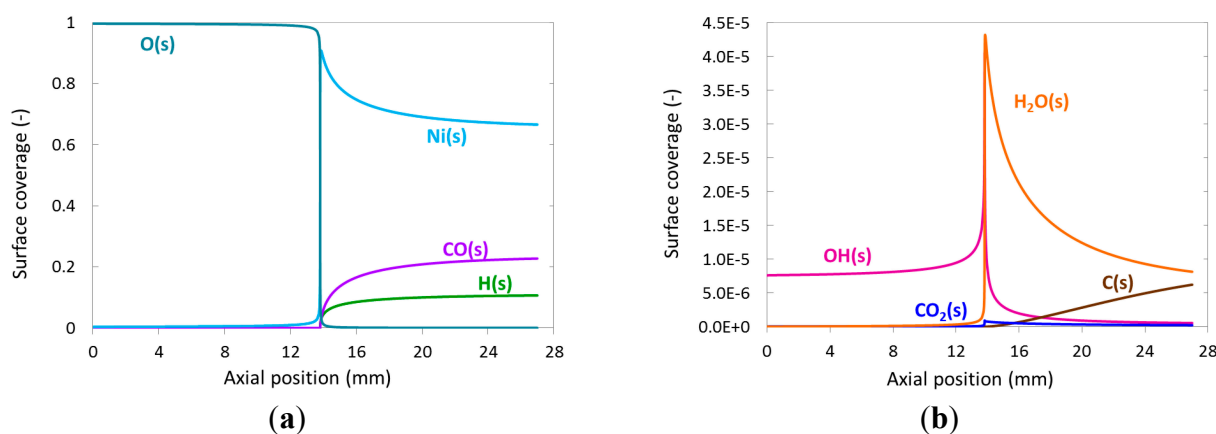
Figure 5. Computed surface coverage of adsorbed species: (**a**) O(s), CO(s), H(s), Ni; (**b**) OH(s), H_2O(s), CO_2(s), and C(s) along the catalytic bed at 973 K, 4 slpm $CH_4/O_2 = 1.6$ and 1 bar.

Sensitivity analysis of the reaction mechanism was carried out at two different temperatures: 723 K (before ignition) and 973 K (after ignition) with $CH_4/O_2 = 1.6$ in nitrogen dilution. The sensitivities of the gas-phase concentrations of CH_4, CO_2, H_2O, H_2 and CO at the outlet of the bed were analyzed by perturbing the pre-exponentials of each reaction. Results for the CO mole fraction, presented in Figure 6, show that for both temperatures the system is highly sensitive to methane adsorption/desorption (R11–R12) along with CH_4(s) dissociation with oxygen assistance (R21) and CO_2 desorption (R8). At 723K, where the total oxidation takes place, the reactions to produce OH(s) and H_2O(s) species (R30–R32) observed to become sensitive due to the availability surface oxygen compared to high temperature region, where oxygen is consumed. The reactions of CO_2 dissociation (R42) and CO desorption (R10) are the most sensitive and are rate determining steps for the production of CO at the high temperature.
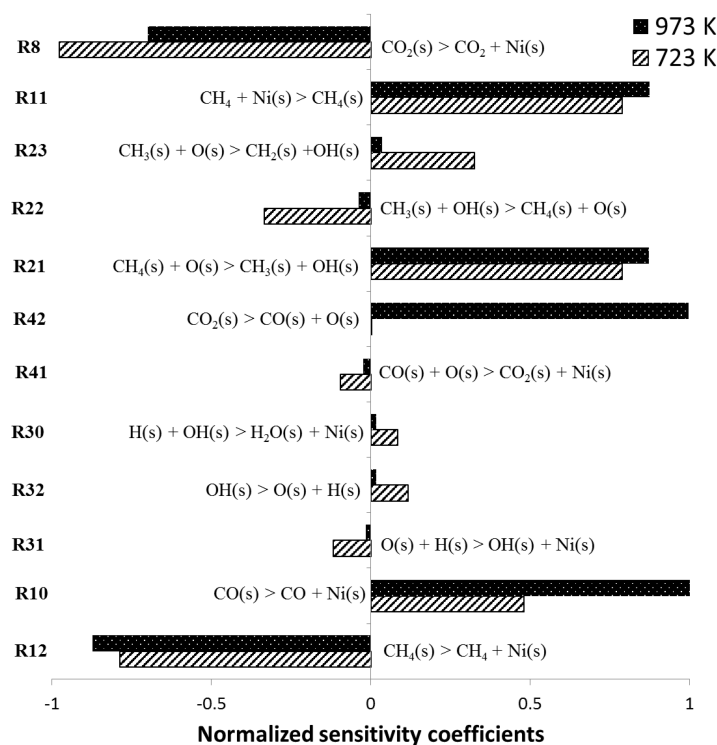
Figure 6. Sensitivity analysis of CO gas-phase concentration for Catalytic Partial Oxidation (CPOX) reaction at 723 K and 948 K.

5.2. Methane Steam Reforming (SR)

A kinetic study of steam reforming of methane over Ni/Al_2O_3 coated monoliths was presented in our previous work including the establishment of a multi-step reaction mechanism [46]. This SR mechanism was successfully applied in studies of steam reforming of methane over, Ni/YSZ anodes of solid oxide fuels cells [99–104], and experimental results from literature [105]. Despite the introduction of new reaction paths, together with adjustments of the kinetic parameters for partial oxidation and dry reforming of methane, the current mechanism extension is still able to predict the experimental results for methane steam reforming. For the evaluation of the newly developed kinetic model, additional experiments were conducted in a fixed bed reactor.

Experimentally determined and computed species concentrations are shown as function of the temperature in a fixed bed reactor in Figure 7. A small amount of CO_2 as a product was observed at temperatures between 623 and 973 K due to the availability of OH(s) species on the surface, originating from the dissociation of water (Figure 7c).

For the sake of clarity we investigate on the validity of the chosen one-dimensional reactor model and the computed reactor outlet concentrations, by roughly estimating the influence of the radial temperature gradient based on the Mears criterion [106] for radial isothermicity. To estimate this effect it is necessary to calculate the radial heat-transfer over the bed cross section. We apply this criterion for the steam reforming inlet gas mixture, which imposes the most critical condition of all experiments in this study, due to the high endothermic value of the heat of reaction amongst the processes considered herein. In reality these harsh conditions are diminished by the coupled water-gas shift reaction which is exothermic in nature.
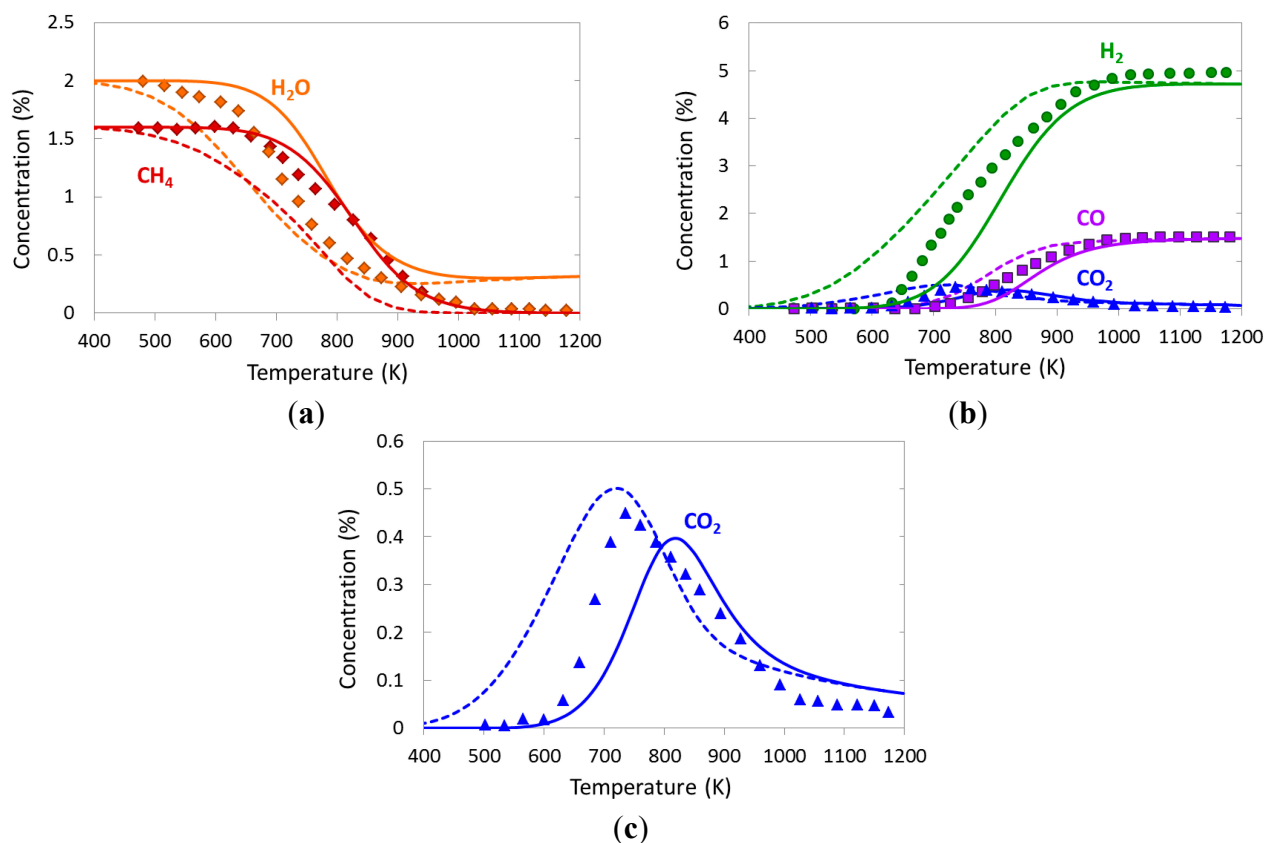
Figure 7. Comparison of experimentally determined (symbols) and numerically predicted (lines) concentrations as a function of temperature for catalytic steam reforming of methane: (**a**) reactants; (**b**) products; (**c**) zoom-in of CO_2 formation; C/S = 0.8 in N_2, 1 bar; T_{inlet} = 373 K; total flow rate of 4 slpm, dashed lines = equilibrium composition at given temperature.

For a reactor feed temperature of 800 K we estimate a radial temperature difference of about 28.5 K. It can be concluded that the simplification of the used one-dimensional packed-bed model assuming isothermal conditions over the bed cross section introduces an error in the simulated species concentrations. This error gives an explanation for the deviation of simulated and measured concentrations as shown in Figure 7. However, since the kinetics of the SR mechanism has been tested separately against experimental data from a monolithic reactor configuration under steam reforming conditions [46], it remains reasonably and simulated concentrations are expected to match experimentally measured ones closer, if instead of a one-dimensional model a two-dimensional packed-bed model is used.

In the present study, reaction flow analysis is performed at 823 K were the maximum CO_2 formation is observed. It can be seen that CO_2 production is preferred through the direct oxidation of CO(s) with O(s) in comparison with the carboxyl path (Figure 8).
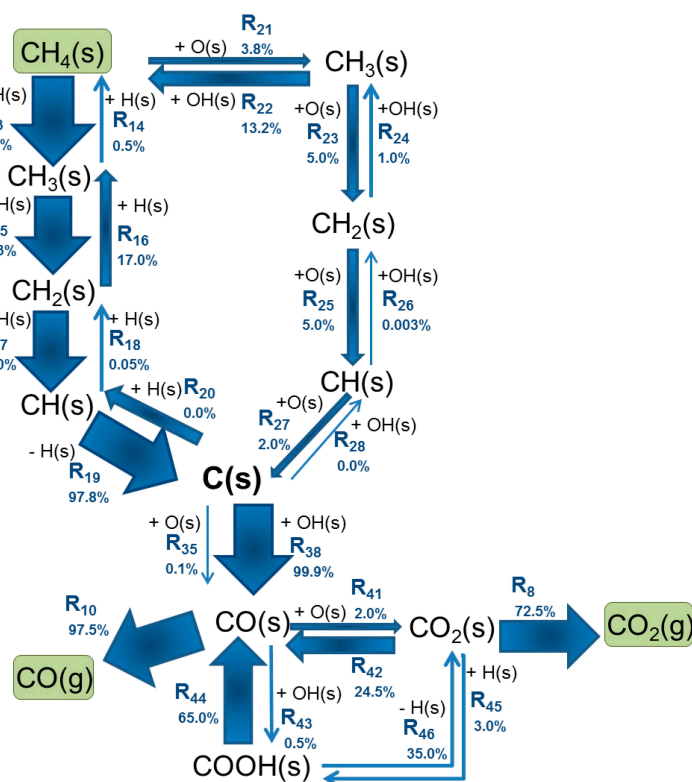
Figure 8. Reaction flow analysis for steam reforming of methane on nickel at 823 K, 1 bar, and a ratio of $CH_4/H_2O = 0.8$.
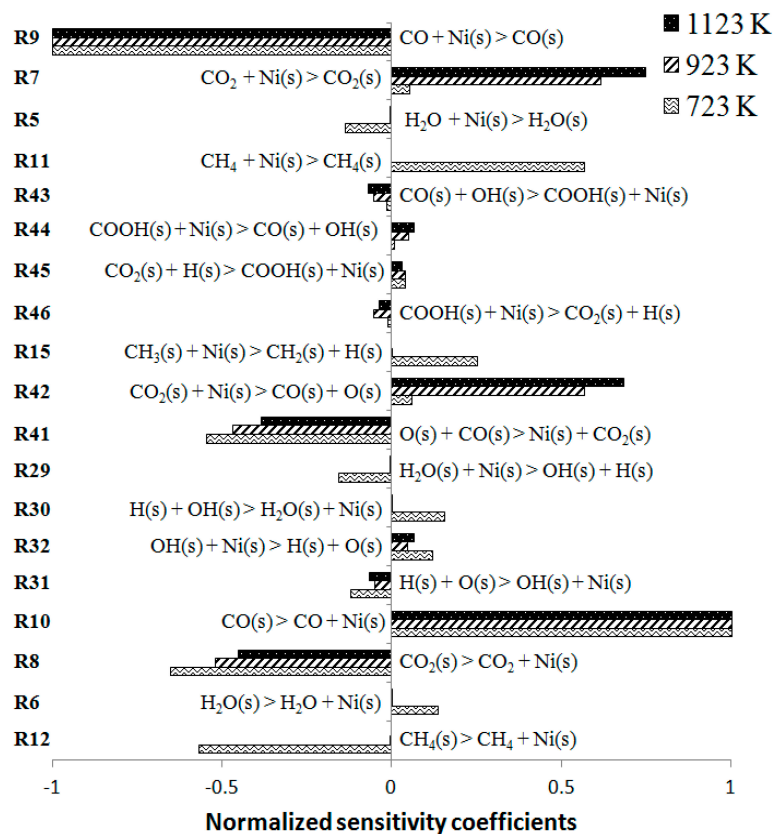
Figure 9. Sensitivity analysis of CO gas-phase concentration for steam reforming methane at different temperatures for $CH_4/H_2O = 0.8$ and 1 bar.

Figure 9 shows the normalized sensitivity coefficients on the CO yield at 723 K, 923 K, and 1123 K for an inlet methane to steam feed ratio (CH_4/H_2O) of 0.8 and at 1 bar. It can be observed that the CO adsorption (R9) and desorption (R10) are highly sensitive as expected for all the reported temperatures. Additionally, at low temperatures (723 K), the CO yield is sensitive to both H_2O adsorption (R5) and desorption (R6) as well as elementary reaction steps of the WGS reaction (R29) and (R30). Besides, adsorption (R11), desorption (R12) and dehydrogenation of methane (R15) play a sensitive role in CO formation. CO_2 dissociation (R42) becomes a sensitive step at high temperatures (823 and 923 K).

5.3. Methane Dry Reforming (DR)

Methane reforming with CO_2 was also studied in the fixed bed reactor. The experimentally measured and computed concentrations of the gas-phase species (CH_4, CO_2, CO, H_2, and H_2O) at the reactor outlet are close to equilibrium for the entire temperature range (Figure 10).

Figure 11 shows the most sensitive reactions for methane conversion by dry reforming, steam reforming and partial oxidation with respect to the rate constant at 1073 K. It can be seen that methane adsorption (R11) and desorption (R12) reactions are the most sensitive reactions for DR and CPOX, while oxygen-assisted dehydrogenation of CH_4 (R21) becomes the most sensitive step for steam reforming. The results indicate that pyrolytic methane dehydrogenation (R13) is sensitive only for dry reforming. However, oxygen-assisted dehydrogenation of methane (R21) is a sensitive step for all processes at 1073 K, in particular for partial oxidation.
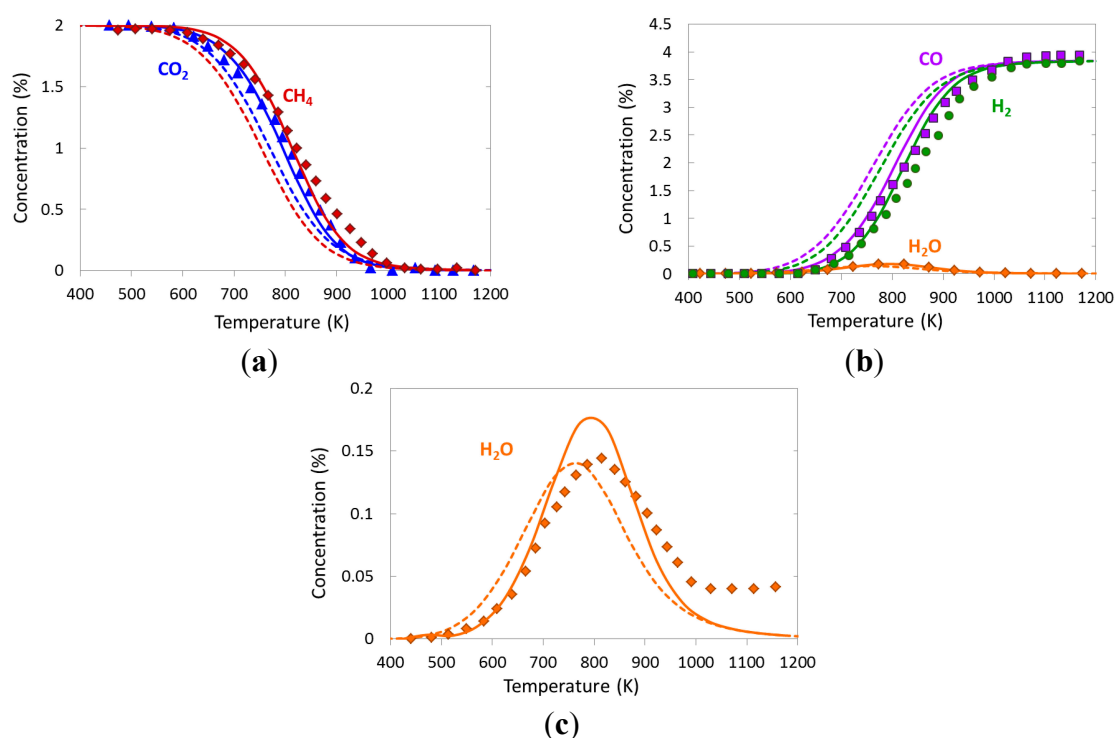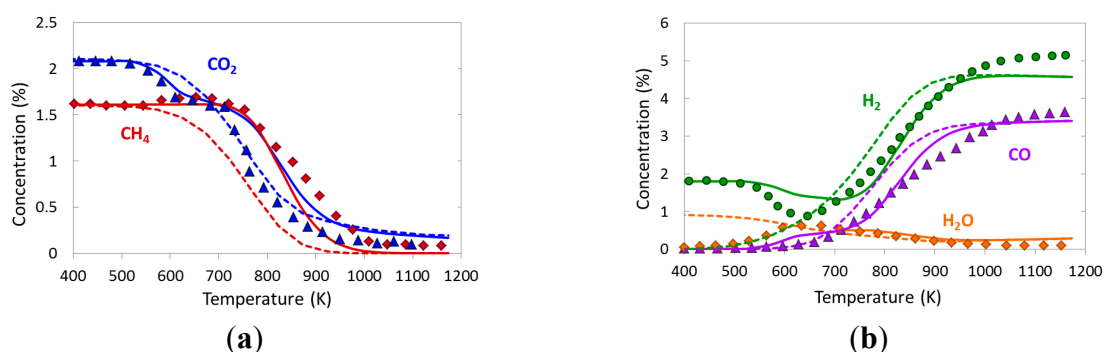

Figure 10. Comparison of experimentally determined (symbols) and numerically predicted (lines) concentrations as a function of temperature for catalytic reforming of methane with CO_2: (**a**) reactants; (**b**) products; (**c**) zoom-in H_2O formation; for $CH_4/CO_2 = 1$ in N_2; 1 bar; $T_{inlet} = 373$ K; total flow rate of 4 slpm, dashed lines = equilibrium composition at given temperature.
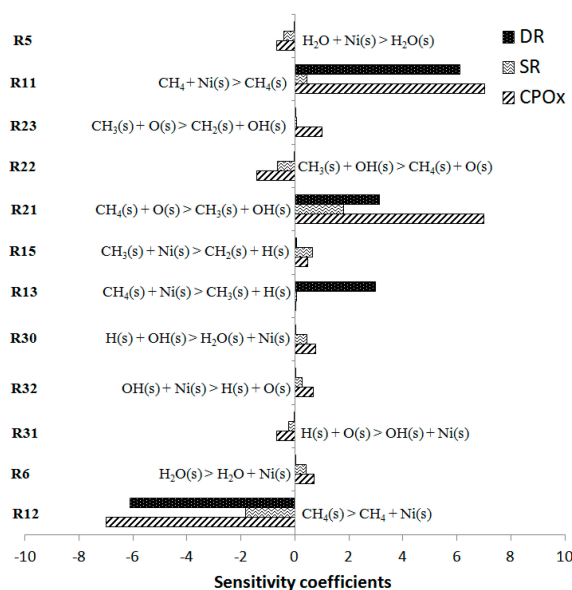
Figure 11. Sensitivity coefficients for CH_4 at 1073 K at DR, SR and CPOX conditions.

## 5.4. Influence of H_2 and H_2O on Methane Reforming with CO_2

As mentioned above, one of the main problems in many industrial reactors that involve methane as fuel is coke deposition on catalysts and the reactor pipe walls. The formation of coke can lead to lower catalytic activity and even complete catalyst deactivation, depending on the amount of solid carbon deposited on the surface [22–26]. Hydrogen and water have recently been studied as inhibitors of coke formation in dry reforming of methane at higher pressure and temperatures [26]. The influence of hydrogen and water in DR of methane was studied in the fixed bed reactor at atmospheric pressure, 4 slpm flow rate, residence time of 0.013 s, temperatures between 373 and 1173 K and inlet mixture of 1.6% CH_4, 2.1% CO_2 and 1.8% H_2 in N_2 dilution. Hydrogen addition led to an increase of water at a lower temperature compared to dry reforming (Figure 12). This water was produced through the RWGS reaching a maximum at 673 K (Figure 12b). As the temperature increases, the water was consumed together with unconverted methane due to the steam reforming reaction.
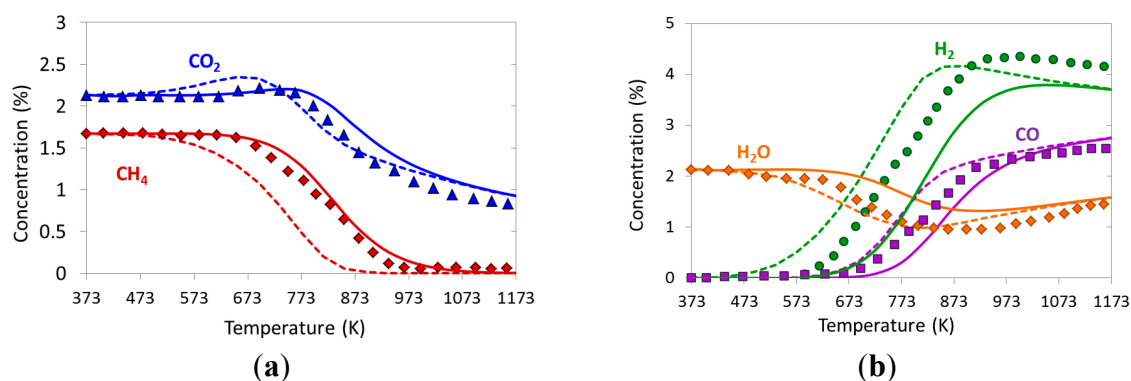

Figure 12. Comparison of experimentally determined (symbols) and numerically predicted (lines) concentrations as a function of temperature for catalytic dry reforming of methane with co-feed H_2: (**a**) CH_4 and CO_2; (**b**) H_2O, CO, H_2, inlet gas composition of 1.6 vol.% CH_4, 2.1 vol.% CO_2, 1.8 vol.% H_2 in N_2; 1 bar; T_{inlet} = 373 K; total flow rate of 4 slpm; dashed lines = equilibrium composition at given temperature.

The computed surface coverage reveals a high coverage with hydrogen and CO at low and medium temperatures respectively (Figure 13). The maximum formation of carbon C(s) is a temperatures between 373 and 573 K, mainly produced by the reaction between CO(s) and H(s) (R37) at low temperature. At higher temperature the total coverage with adsorbed species is rather low.

In Figure 14, the experimental and numerical results are given for dry reforming with steam as co-feed. At temperatures between 723 and 823 K, some additional CO_2 was produced, by the WGS reaction.
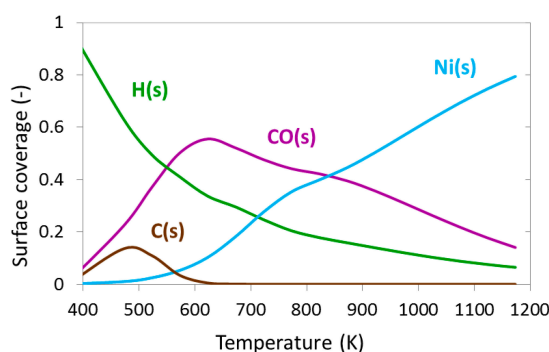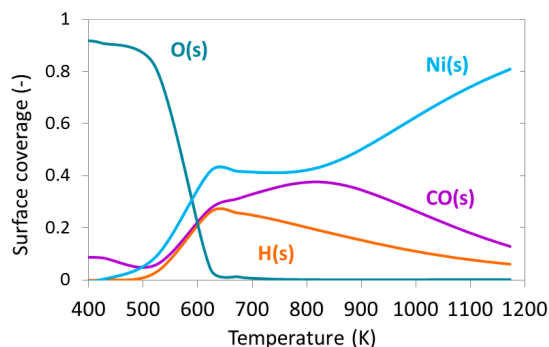

Figure 13. Computed surface coverage of adsorbed species as function of the temperature for methane dry reforming with H_2 co-feed: inlet gas composition of 1.6 vol.% CH_4, 2.1 vol.% CO_2, 1.8 vol.% H_2 in N_2; 1 bar; total flow rate 4 slpm.


Figure 14. Comparison of experimentally determined (symbols) and numerically predicted (lines) concentrations as a function of temperature for catalytic dry reforming of methane with co-feed H_2O: (**a**) CH_4, and CO_2; (**b**) H_2O, CO, H_2, inlet gas composition of 1.7 vol.% CH_4, 2.1 vol.% CO_2, 2.1 vol.% H_2O in N_2; 1 bar; T_{inlet} = 373 K, total flow rate of 4 slpm, dashed lines = equilibrium composition at given temperature.

In the intermediate temperature range, the outlet stream has not reached the equilibrium composition yet. At temperatures below 523 K, the surface was mainly covered by oxygen coming from H_2O(s) dissociation in the simulation (Figure 15). As the temperature increases the oxygen coverage decreases rapidly leading to vacant nickel sites and H(s) and CO(s) become the most abundant surface intermediates. No significant concentration of surface carbon was observed at low temperatures in comparison with the previous results using H_2 as co-feed (Figure 15).

During the experiments performed in this study, no formation of visible carbon deposits on the surface was observed at all operations conditions. Nevertheless, a comparison of the computed carbon coverage at the three different conditions studied for DR reveals the inhibition of $C(s)$ formation by H_2 and H_2O (Figure 16).


Figure 15. Computed surface coverage of adsorbed species as function of the temperature for methane dry reforming with H_2O co-feed: 1.7 vol.% CH_4, 2.1 vol.% CO_2, 2.1 vol.% H_2O in N_2; 1 bar; $T_{inlet} = 373$ K; total flow rate of 4 slpm.
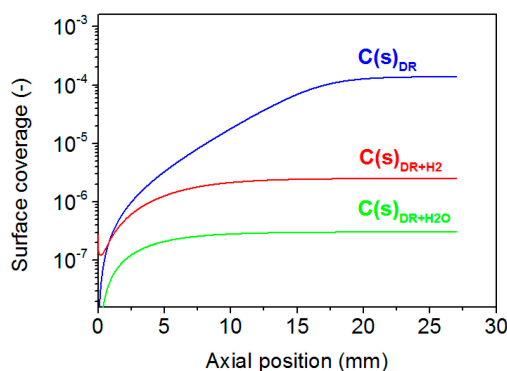
Figure 16. Computed surface coverage for carbon along the catalytic bed for methane reforming with CO_2 at 1123 K: (**a**) comparison of methane dry reforming without and with H_2, and H_2O co-feed respectively.

Figure 17 describes the most sensitive reactions for carbon formation during dry reforming in presence of H_2 and H_2O at 1123 K. Addition of both H_2O and H_2 make the reactions (R37) and (R38) highly sensitive. It can be seen that adsorption/desorption of CO_2 (R7, R8) are very sensitive reactions in the presence of H_2O as well as CO_2 dissociation (R42) and CO_2 formation thought the direct oxidation of $CO(s)$ with $O(s)$ (R41). Besides, direct oxidation of $CO(s)$ (R41), $CO(s)$ is also oxidized with $OH(s)$ (R43) to produce $CO_2(s)$ involving the $COOH(s)$ path (R46). The results also indicate that in the presence of H_2 as co-feed for the DR, water adsorption (R5) and desorption (R6) become sensitive reactions as well as $H_2O(s)$ formation (R30) and dissociation (R29). In both cases, either by the addition of hydrogen or water, the formation (R31) and dissociation of $OH(s)$ (R32) becomes rate determining steps. This is the case, because $OH(s)$ is the main oxidant for $C(s)$ in the system.
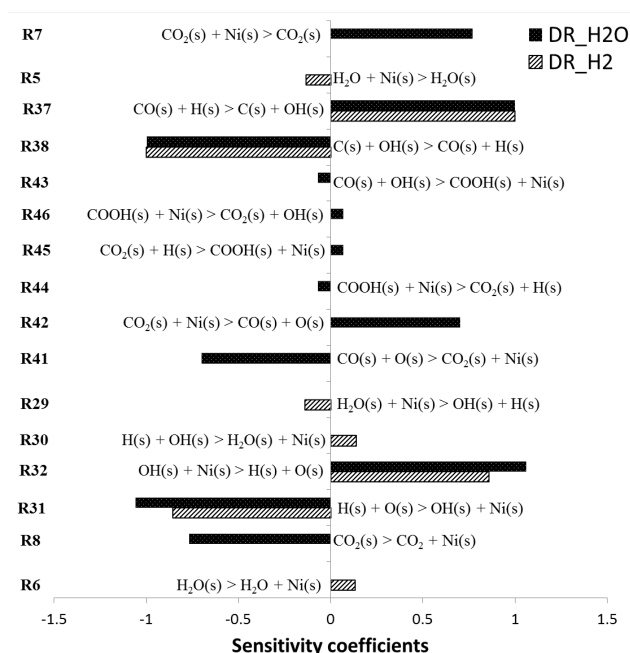
Figure 17. Sensitivity analysis of C(s) formation for dry reforming in the presence of H_2 and H_2O at 1123 K.

6. Summary

The kinetics of oxidation and reforming of methane over nickel were studied experimentally and numerically. Experimental investigations for partial oxidation dry and steam reforming of methane were performed in a flow reactor over a powdered Ni-based catalyst. A detailed reaction mechanism for the catalytic conversion of methane under oxidative and reforming conditions was developed and evaluated by comparison of experimentally derived and numerically predicted conversion and selectivity. The mechanism was implemented into a one-dimensional flow field description of a fixed bed reactor. A new numerical adjustment procedure was applied through the development process to ensure the overall thermodynamic consistency of the mechanism.

The newly developed kinetic model makes it possible to predict the product distribution for partial oxidation and reforming of methane as well as the impact of the co-feed of products such as hydrogen and water on the dry reforming process. Furthermore, the simulation tools developed allow the numerical simulation of chemical species profiles and surface coverage within the catalytic bed.

Experimental and numerical results for synthesis gas production via partial oxidation of methane are consistent with the indirect path where the total oxidation of methane takes place, first producing CO_2 and H_2O, which react with the remaining methane through reforming reactions to produce H_2 and CO.

Experimental results where H_2O and H_2 are co-fed together with methane and CO_2 show that both H_2O and H_2 act as inhibitors for coke deposition. The numerical simulations reveal a significant decrease in surface carbon concentration during reaction conditions where H_2 and H_2O were added as co-reactants. However, H_2O provides a better inhibition effect than H_2 on the catalytic surface.

The model developed can be extended for industrial applications, quantitatively predicting the effect of inlet compositions, operating conditions and undesirable transient modifications of the active catalytic phase, e.g., by deactivation and coking, which are the main challenge in industrial catalytic reformers.

Future work will focus on the implementation of a coking model in the surface reaction scheme to describe transient carbon deposition on the surface.

Author Contributions

K. Herrera Delgado did the simulation and experimental work, did the development of new extended version of the mechanism, wrote the paper, answered the questions of the reviewers, made editing and improvement corrections of manuscript; L. Maier proposed the idea, developed the first version of the mechanism and supervised their extension and revision, proposed the experiments for mechanism evaluation, answered the questions of the reviewers, made editing and improvement corrections of manuscript; S. Tischer developed the procedure and computer code for thermodynamic consistency, wrote appropriate part of the manuscript; A. Zellner did technical support on experimental layout, performed some experiments; H. Stotz made the estimation of the isothermcity of the reactor, wrote appropriate statement to the model description, helped in addressing the reviewer's questions, made editing and corrections of the manuscript; O. Deutschmann is a supervisor, worked on all topics listed above.

Conflicts of Interest

The authors declare no conflict of interest.

References

1. Rostrup-Nielsen, J.; Dybkjaer, I.; Aasberg-Petersen, K. Synthesis gas for large scale fischer-tropsch synthesis. *Am. Chem. Soc. Div. Pet. Chem. Prepr.* **2000**, *45*, 186–189.
2. Rostrup-Nielsen, J.R.; Sehested, J.; Nørskov, J.K. Hydrogen and synthesis gas by steam- and CO_2 reforming. In *Advances in Catalysis*; Elsevier: Amherst, MA, USA, 2002; Volume 47, pp. 65–139.
3. Iglesia, E. Design, synthesis, and use of cobalt-based fischer-tropsch synthesis catalysts. *Appl. Catal. A* **1997**, *161*, 59–78.
4. Rostrup-Nielsen, J.R. New aspects of syngas production and use. *Catal. Today* **2000**, *63*, 159–164.
5. Hickman, D.A.; Schmidt, L.D. Production of syngas by direct catalytic oxidation of methane. *Science* **1993**, *259*, 343–346.
6. Peña, M.A.; Gómez, J.P.; Fierro, J.L.G. New catalytic routes for syngas and hydrogen production. *Appl. Catal. A* **1996**, *144*, 7–57.
7. Shao, Z.; Haile, S.M. A high-performance cathode for the next generation of solid-oxide fuel cells. *Nature* **2004**, *431*, 170–173.

8. Park, S.; Vohs, J.M.; Gorte, R.J. Direct oxidation of hydrocarbons in a solid-oxide fuel cell. *Nature* **2000**, *404*, 265–267.

9. Singhal, S.C. Advances in solid oxide fuel cell technology. *Solid State Ionics* **2000**, *135*, 305–313.

10. Aparicio, L.M. Transient isotopic studies and microkinetic modeling of methane reforming over nickel catalysts. *J. Catal.* **1997**, *165*, 262–274.

11. Xu, J.; Froment, G.F. Methane steam reforming, methanation and water-gas shift: I. Intrinsic kinetics. *AIChE J.* **1989**, *35*, 88–96.

12. Rostrup-Nielsen, J. Catalytic Steam Reforming. In *Catalysis*; Anderson, J., Boudart, M., Eds.; Springer: Berlin/Heidelberg, Germany, 1984; Volume 5, pp. 1–117.

13. Bradford, M.C.J.; Vannice, M.A. CO_2 reforming of ch_4. *Catal. Rev.* **1999**, *41*, 1–42.

14. Zhu, Y.-A.; Chen, D.; Zhou, X.-G.; Yuan, W.-K. DFT studies of dry reforming of methane on Ni catalyst. *Catal. Today* **2009**, *148*, 260–267.

15. Dissanayake, D.; Rosynek, M.P.; Kharas, K.C.C.; Lunsford, J.H. Partial oxidation of methane to carbon monoxide and hydrogen over a Ni/Al_2O_3 catalyst. *J. Catal.* **1991**, *132*, 117–127.

16. Zhu, T.; Flytzani-Stephanopoulos, M. Catalytic partial oxidation of methane to synthesis gas over $Ni–CeO_2$. *Appl. Catal. A* **2001**, *208*, 403–417.

17. Tang, S.; Lin, J.; Tan, K.L. Partial oxidation of methane to syngas over Ni/MgO, Ni/CaO and Ni/CeO_2. *Catal. Lett.* **1998**, *51*, 169–175.

18. Goula, M.A.; Lemonidou, A.A.; Grünert, W.; Baerns, M. Methane partial oxidation to synthesis gas using nickel on calcium aluminate catalysts. *Catal. Today* **1996**, *32*, 149–156.

19. Liu, Z.-W.; Jun, K.-W.; Roh, H.-S.; Park, S.-E.; Oh, Y.-S. Partial oxidation of methane over nickel catalysts supported on various aluminas. *Korean J. Chem. Eng.* **2002**, *19*, 735–741.

20. Vernon, P.F.; Green, M.H.; Cheetham, A.; Ashcroft, A. Partial oxidation of methane to synthesis gas. *Catal. Lett.* **1990**, *6*, 181–186.

21. Li, C.; Yu, C.; Shen, S. Role of the surface state of Ni/Al_2O_3 in partial oxidation of CH_4. *Catal. Lett.* **2000**, *67*, 139–145.

22. Rostrup-Nielsen, J.R. Sulfur-passivated nickel-catalysts for carbon-free steam reforming of methane. *J. Catal.* **1984**, *85*, 31–43.

23. Trimm, D.L. Formation and removal of coke from nickel-catalyst. *Catal. Rev. Sci. Eng.* **1977**, *16*, 155–189.

24. Bartholomew, C.H. Carbon deposition in steam reforming and methanation. *Catal. Rev.* **1982**, *24*, 67–112.

25. Blekkan, E.A.; Myrstad, R.; Olsvik, O.; Rokstad, O.A. Characterization of tars and coke formed during the pyrolysis of methane in a tubular reactor. *Carbon* **1992**, *30*, 665–673.

26. Kahle, L.C.S.; Roussière, T.; Maier, L.; Herrera Delgado, K.; Wasserschaff, G.; Schunk, S.A.; Deutschmann, O. Methane dry reforming at high temperature and elevated pressure: Impact of gas-phase reactions. *Ind. Eng. Chem. Res.* **2013**, *52*, 11920–11930.

27. Wang, S.; Lu, G.Q.M. CO_2 reforming of methane on Ni catalysts: Effects of the support phase and preparation technique. *Appl. Catal. B* **1998**, *16*, 269–277.

28. Ross, J.R.H.; vanKeulen, A.N.J.; Hegarty, M.E.S.; Seshan, K. The catalytic conversion of natural gas to useful products. *Catal. Today* **1996**, *30*, 193–199.

29. Ginsburg, J.M.; Pina, J.; El Solh, T.; de Lasa, H.I. Coke formation over a nickel catalyst under methane dry reforming conditions: Thermodynamic and kinetic models. *Ind. Eng. Chem. Res.* **2005**, *44*, 4846–4854.

30. Guo, J.; Lou, H.; Zheng, X.M. The deposition of coke from methane on a $Ni/MgAl_2O_4$ catalyst. *Carbon* **2007**, *45*, 1314–1321.

31. Chen, D.; Lodeng, R.; Anundskas, A.; Olsvik, O.; Holmen, A. Deactivation during carbon dioxide reforming of methane over ni catalyst: Microkinetic analysis. *Chem. Eng. Sci.* **2001**, *56*, 1371–1379.

32. Chen, D.; Lødeng, R.; Svendsen, H.; Holmen, A. Hierarchical multiscale modeling of methane steam reforming reactions. *Ind. Eng. Chem. Res.* **2010**, *50*, 2600–2612.

33. Kunz, L.; Maier, L.; Tischer, S.; Deutschmann, O. Modeling the rate of heterogeneous reactions. In *Modeling and Simulation of Heterogeneous Catalytic Reactions*; Wiley-VCH Verlag GmbH & Co. KGaA: Weinheim, Germany, 2011; pp. 113–148.

34. Mhadeshwar, A.B.; Vlachos, D.G. Hierarchical multiscale mechanism development for methane partial oxidation and reforming and for thermal decomposition of oxygenates on Rh. *J. Phys. Chem. B* **2005**, *109*, 16819–16835.

35. Wei, J.; Iglesia, E. Isotopic and kinetic assessment of the mechanism of reactions of CH_4 with CO_2 or H_2O to form synthesis gas and carbon on nickel catalysts. *J. Catal.* **2004**, *224*, 370–383.

36. Blaylock, D.W.; Zhu, Y.-A.; Green, W. Computational investigation of the thermochemistry and kinetics of steam methane reforming over a multi-faceted nickel catalyst. *Top. Catal.* **2011**, *54*, 828–844.

37. Blaylock, D.W.; Ogura, T.; Green, W.H.; Beran, G.J.O. Computational investigation of thermochemistry and kinetics of steam methane reforming on Ni(111) under realistic conditions. *J. Phys. Chem. C* **2009**, *113*, 4898–4908.

38. Wang, S.-G.; Liao, X.-Y.; Hu, J.; Cao, D.-B.; Li, Y.-W.; Wang, J.; Jiao, H. Kinetic aspect of CO_2 reforming of CH_4 on Ni(111): A density functional theory calculation. *Surf. Sci.* **2007**, *601*, 1271–1284.

39. Schwiedernoch, R.; Tischer, S.; Correa, C.; Deutschmann, O. Experimental and numerical study on the transient behavior of partial oxidation of methane in a catalytic, monolith. *Chem. Eng. Sci.* **2003**, *58*, 633–642.

40. Nogare, D.D.; Degenstein, N.J.; Horn, R.; Canu, P.; Schmidt, L.D. Modeling spatially resolved data of methane catalytic partial oxidation on Rh foam catalyst at different inlet compositions and flowrates. *J. Catal.* **2011**, *277*, 134–148.

41. Diehm, C.; Deutschmann, O. Hydrogen production by catalytic partial oxidation of methane over staged Pd/Rh coated monoliths: Spatially resolved concentration and temperature profiles. *Int. J. Hydrog. Energy* **2014**, *39*, 17998–18004.

42. Horn, R.; Williams, K.A.; Degenstein, N.J.; Bitsch-Larsen, A.; Dalle Nogare, D.; Tupy, S.A.; Schmidt, L.D. Methane catalytic partial oxidation on autothermal Rh and Pt foam catalysts: Oxidation and reforming zones, transport effects, and approach to thermodynamic equilibrium. *J. Catal.* **2007**, *249*, 380–393.

43. Donazzi, A.; Beretta, A.; Groppi, G.; Forzatti, P. Catalytic partial oxidation of methane over a 4% $Rh/\alpha-Al_2O_3$ catalyst: Part i: Kinetic study in annular reactor. *J. Catal.* **2008**, *255*, 241–258.

44. Christian Enger, B.; Lødeng, R.; Holmen, A. A review of catalytic partial oxidation of methane to synthesis gas with emphasis on reaction mechanisms over transition metal catalysts. *Appl. Catal. A* **2008**, *346*, 1–27.

45. De Groote, A.M.; Froment, G.F.; Kobylinski, T. Synthesis gas production from natural gas in a fixed bed reactor with reversed flow. *Can. J. Chem. Eng.* **1996**, *74*, 735–742.

46. Maier, L.; Schädel, B.; Herrera Delgado, K.; Tischer, S.; Deutschmann, O. Steam reforming of methane over nickel: Development of a multi-step surface reaction mechanism. *Top. Catal.* **2011**, *54*, 845–858.

47. Hartmann, M.; Maier, L.; Minh, H.D.; Deutschmann, O. Catalytic partial oxidation of iso-octane over rhodium catalysts: An experimental, modeling, and simulation study. *Combust. Flame* **2010**, *157*, 1771–1782.™

48. Deutschmann, O.; Tischer, S.; Kleditzsch, S.; Janardhanan, V.M.; Correa, C.; Chatterjee, D.; Mladenov, N.; Minh, H.D. DETCHEM™ software package. Available online: www.detchem.com (accessed on 26 May 2015).

49. Pushnov, A.S. Calculation of average bed porosity. *Chem. Petrol. Eng.* **2006**, *42*, 14–17.

50. Deutschmann, O. Computational Fluid Dynamics Simulation of Catalytic Reactors. In *Handbook of Heterogeneous Catalysis*; Erlt, H.K.G., Schüth, F., Weitkamp, J., Eds.; Wiley-VCH Verlag GmbH & Co. KGaA: Weinheim, Germany, 2008; pp. 1811–1828.

51. Kee, R.J.; Coltrin, M.E.; Glarborg, P. Heterogeneous chemistry. In *Chemically Reacting Flow*; John Wiley & Sons, Inc.: Hoboken, NJ, USA, 2005; pp. 445–486.

52. Mhadeshwar, A.B.; Vlachos, D.G. A thermodynamically consistent surface reaction mechanism for co oxidation on pt. *Combust. Flame* **2005**, *142*, 289–298.

53. Lee, M.B.; Yang, Q.Y.; Tang, S.L.; Ceyer, S.T. Activated dissociative chemisorption of CH_4 on Ni(111): Observation of a methyl radical and implication for the pressure gap in catalysis. *J. Chem. Phys.* **1986**, *85*, 1693.

54. Shustorovich, E. *The Bond-Order Conservation Approach to Chemisorption and Heterogeneous Catalysis: Applications and Implications*; WILEY-VCH Verlag GmbH & Co. KgaA: Weinheim, Germany, 1991; Volume 22, pp. 1522–2667.

55. Sellers, H. The generalized ubi-qep method for modeling the energetics of reactions on transition metal surfaces. *Surf. Sci.* **2003**, *524*, 29–39.

56. Qin, D.; Lapszewicz, J.; Jiang, X. Comparison of partial oxidation and steam-CO_2 mixed reformingof CH_4 to syngas on MgO-supported metals. *J. Catal.* **1996**, *159*, 140–149.

57. Bartholomew, C. Hydrogen adsorption on supported cobalt, iron, and nickel. *Catal. Lett.* **1990**, *7*, 27–51.

58. Weatherbee, G.D.; Bartholomew, C.H. Effects of support on hydrogen adsorption/desorption kinetics of nickel. *J. Catal.* **1984**, *87*, 55–65.

59. Kratzer, P.; Hammer, B.; Norskov, J.K. A theoretical study of CH_4 dissociation on pure and gold-alloyed Ni(111) surfaces. *J. Chem. Phys.* **1996**, *105*, 5595–5604.

60. Zhu, X.Y.; White, J.M. Hydrogen interaction with nickel (100): A static secondary ion mass spectroscopy study. *J. Phys. Chem.* **1988**, *92*, 3970–3974.

61. Bengaard, H.S.; Nørskov, J.K.; Sehested, J.; Clausen, B.S.; Nielsen, L.P.; Molenbroek, A.M.; Rostrup-Nielsen, J.R. Steam reforming and graphite formation on Ni catalysts. *J. Catal.* **2002**, *209*, 365–384.

62. Stuckless, J.T.; Wartnaby, C.E.; Al-Sarraf, N.; Dixon-Warren, S.J.B.; Kovar, M.; King, D.A. Oxygen chemisorption and oxide film growth on Ni{100}, {110}, and {111}: Sticking probabilities and microcalorimetric adsorption heats. *J. Chem. Phys.* **1997**, *106*, 2012–2030.

63. Siegbahn, P.E.M.; Wahlgren, U. A theoretical study of atomic oxygen chemisorption on the Ni(100) and Ni(111) surfaces. *Int. J. Quantum Chem.* **1992**, *42*, 1149–1169.

64. Stulen, R.H.; Thiel, P.A. Electron-stimulated desorption and thermal desorption spectrometry of H_2O on nickel (111). *Surf. Sci* **1985**, *157*, 99–118.

65. Pache, T.; Steinrück, H.P.; Huber, W.; Menzel, D. The adsorption of H_2O on clean and oxygen precovered Ni(111) studied by arups and tpd. *Surf. Sci.* **1989**, *224*, 195–214.

66. Zakharov, I.I.; Avdeev, V.I.; Zhidomirov, G.M. Non-empirical cluster model calculations of the adsorption of H_2O on Ni(111). *Surf. Sci.* **1992**, *277*, 407–413.

67. Shustorovich, E.; Sellers, H. The UBI-QEP method: A practical theoretical approach to understanding chemistry on transition metal surfaces. *Surf. Sci. Rep.* **1998**, *31*, 1–119.

68. Shustorovich, E. Reaction Energetics on Transition Metal Surfaces: A Bond-Order Conservation Approach. In *Quantum Chemistry Approaches to Chemisorption and Heterogeneous Catalysis*; Ruette, F., Ed.; Springer: Dordrecht, The Netherlands, 1992; Volume 6, pp. 231–252.

69. Bjorgum, E.; Chen, D.; Bakken, M.G.; Christensen, K.O.; Holmen, A.; Lytken, O.; Chorkendorff, I. Energetic mapping of ni catalysts by detailed kinetic modeling. *J. Phys. Chem. B* **2005**, *109*, 2360–2370.

70. Al-Sarraf, N.; Stuckless, J.T.; Wartnaby, C.E.; King, D.A. Adsorption microcalorimetry and sticking probabilities on metal single crystal surfaces. *Surf. Sci.* **1993**, *283*, 427–437.

71. Chan, D.; Tischer, S.; Heck, J.; Diehm, C.; Deutschmann, O. Correlation between catalytic activity and catalytic surface area of a Pt/Al_2O_3 doc: An experimental and microkinetic modeling study. *Appl. Catal. B* **2014**, *156–157*, 153–165.

72. Jacobs, G.; Graham, U.M.; Chenu, E.; Patterson, P.M.; Dozier, A.; Davis, B.H. Low-temperature water-gas shift: Impact of Pt promoter loading on the partial reduction of ceria and consequences for catalyst design. *J. Catal.* **2005**, *229*, 499–512.

73. Jacobs, G.; Patterson, P.M.; Williams, L.; Chenu, E.; Sparks, D.; Thomas, G.; Davis, B.H. Water-gas shift: *In situ* spectroscopic studies of noble metal promoted ceria catalysts for co removal in fuel cell reformers and mechanistic implications. *Appl. Catal. A* **2004**, *262*, 177–187.

74. Jacobs, G.; Patterson, P.M.; Graham, U.M.; Sparks, D.E.; Davis, B.H. Low temperature water-gas shift: Kinetic isotope effect observed for decomposition of surface formates for Pt/ceria catalysts. *Appl. Catal. A* **2004**, *269*, 63–73.

75. Jacobs, G.; Patterson, P.M.; Graham, U.M.; Crawford, A.C.; Davis, B.H. Low temperature water gas shift: The link between the catalysis of WGS and formic acid decomposition over Pt/ceria. *Int. J. Hydrog. Energy* **2005**, *30*, 1265–1276.

76. Jacobs, G.; Williams, L.; Graham, U.; Sparks, D.; Davis, B.H. Low-temperature water-gas shift: *In-situ* drifts-reaction study of a Pt/CeO_2 catalyst for fuel cell reformer applications. *J. Phys. Chem. B* **2003**, *107*, 10398–10404.

77. Kalamaras, C.M.; Olympiou, G.G.; Efstathiou, A.M. The water-gas shift reaction on $Pt/\gamma-Al_2O_3$ catalyst: Operando ssitka-drifts-mass spectroscopy studies. *Catal. Today* **2008**, *138*, 228–234.

78. Tibiletti, D.; Goguet, A.; Reid, D.; Meunier, F.C.; Burch, R. On the need to use steady-state or operando techniques to investigate reaction mechanisms: An *in situ* drifts and ssitka-based study example. *Catal. Today* **2006**, *113*, 94–101.

79. Shido, T.; Iwasawa, Y. Reactant-promoted reaction mechanism for water-gas shift reaction on Rh-doped ceo2. *J. Catal.* **1993**, *141*, 71–81.

80. Gokhale, A.A.; Dumesic, J.A.; Mavrikakis, M. On the mechanism of low-temperature water gas shift reaction on copper. *J. Am. Chem. Soc.* **2008**, *130*, 1402–1414.

81. Chen, Y.; Wang, H.; Burch, R.; Hardacre, C.; Hu, P. New insight into mechanisms in water-gas-shift reaction on Au/CeO_2(111): A density functional theory and kinetic study. *Faraday Discuss.* **2011**, *152*, 121–133.

82. Lin, C.-H.; Chen, C.-L.; Wang, J.-H. Mechanistic studies of water–gas-shift reaction on transition metals. *J. Phys. Chem. C* **2011**, *115*, 18582–18588.

83. Boisen, A.; Janssens, T.V.W.; Schumacher, N.; Chorkendorff, I.; Dahl, S. Support effects and catalytic trends for water gas shift activity of transition metals. *J. Mol. Catal. A* **2010**, *315*, 163–170.

84. Grabow, L.C.; Gokhale, A.A.; Evans, S.T.; Dumesic, J.A.; Mavrikakis, M. Mechanism of the water gas shift reaction on Pt: First principles, experiments, and microkinetic modeling. *J. Phys. Chem. C* **2008**, *112*, 4608–4617.

85. Karakaya, C.; Otterstätter, R.; Maier, L.; Deutschmann, O. Kinetics of the water-gas shift reaction over rh/Al_2O_3 catalysts. *Appl. Catal. A* **2014**, *470*, 31–44.

86. Inderwildi, O.R.; Jenkins, S.J.; King, D.A. An unexpected pathway for the catalytic oxidation of methylidyne on Rh(111) as a route to syngas. *J. Am. Chem. Soc.* **2007**, *129*, 1751–1759.

87. Inderwildi, O.R.; Jenkins, S.J.; King, D.A. Mechanistic studies of hydrocarbon combustion and synthesis on noble metals. *Angew. Chem. Int. Ed.* **2008**, *47*, 5253–5255.

88. Pistonesi, C.; Juan, A.; Irigoyen, B.; Amadeo, N. Theoretical and experimental study of methane steam reforming reactions over nickel catalyst. *Appl. Surf. Sci.* **2007**, *253*, 4427–4437.

89. Weng, W.Z.; Chen, M.S.; Yan, Q.G.; Wu, T.H.; Chao, Z.S.; Liao, Y.Y.; Wan, H.L. Mechanistic study of partial oxidation of methane to synthesis gas over supported rhodium and ruthenium catalysts using *in situ* time-resolved FTIR spectroscopy. *Catal. Today* **2000**, *63*, 317–326.

90. Hei, M.J.; Chen, H.B.; Yi, J.; Lin, Y.J.; Lin, Y.Z.; Wei, G.; Liao, D.W. CO_2-reforming of methane on transition metal surfaces. *Surf. Sci.* **1998**, *417*, 82–96.

91. Horn, R.; Williams, K.A.; Degenstein, N.J.; Schmidt, L.D. Syngas by catalytic partial oxidation of methane on rhodium: Mechanistic conclusions from spatially resolved measurements and numerical simulations. *J. Catal.* **2006**, *242*, 92–102.

92. Deutschmann, O.; Schmidt, L.D. Two-dimensional modeling of partial oxidation of methane on rhodium in a short contact time reactor. *Symp. (Int.) Combust.* **1998**, *27*, 2283–2291.

93. Deutschmann, O.; Schmidt, L.D. Modeling the partial oxidation of methane in a short-contact-time reactor. *AIChE J.* **1998**, *44*, 2465–2477.

94. Li, C.; Yu, C.; Shen, S. Isotopic studies on the mechanism of partial oxidation of CH_4 to syngas over a Ni/Al_2O_3 catalyst. *Catal. Lett.* **2001**, *75*, 183–189.

95. Tang, S.; Lin, J.; Tan, K.L. Pulse-ms studies on CH_4/Cd_4 isotope effect in the partial oxidation of methane to syngas over Pt/α-Al_2O_3. *Catal. Lett.* **1998**, *55*, 83–86.

96. Wang, H.Y.; Ruckenstein, E. Catalytic partial oxidation of methane to synthesis gas over γ- Al_2O_2-supported Rhodium catalysts. *Catal. Lett.* **1999**, *59*, 121–127.

97. Kim, S.-B.; Kim, Y.-K.; Lim, Y.-S.; Kim, M.-S.; Hahm, H.-S. Reaction mechanism of partial oxidation of methane to synthesis gas over supported Ni catalysts. *Korean J. Chem. Eng.* **2003**, *20*, 1023–1025.

98. Choudhary, V.R.; Rajput, A.M.; Prabhakar, B. Nonequilibrium oxidative conversion of methane to CO and H_2 with high selectivity and productivity over Ni/Al_2O_3 at low temperatures. *J. Catal.* **1993**, *139*, 326–328.

99. Menon, V.; Janardhanan, V.M.; Tischer, S.; Deutschmann, O. A novel approach to model the transient behavior of solid-oxide fuel cell stacks. *J. Power Sources* **2012**, *214*, 227–238.

100. Menon, V.; Fu, Q.; Janardhanan, V.M.; Deutschmann, O. A model-based understanding of solid-oxide electrolysis cells (soecs) for syngas production by H_2O/CO_2 co-electrolysis. *J. Power Sources* **2015**, *274*, 768–781.

101. Janardhanan, V.M.; Deutschmann, O. CFD analysis of a solid oxide fuel cell with internal reforming: Coupled interactions of transport, heterogeneous catalysis and electrochemical processes. *J. Power Sources* **2006**, *162*, 1192–1202.

102. Bessler, W.G.; Gewies, S.; Vogler, M. A new framework for physically based modeling of solid oxide fuel cells. *Electrochim. Acta* **2007**, *53*, 1782–1800.

103. Hecht, E.S.; Gupta, G.K.; Zhu, H.; Dean, A.M.; Kee, R.J.; Maier, L.; Deutschmann, O. Methane reforming kinetics within a ni–ysz sofc anode support. *Appl. Catal. A* **2005**, *295*, 40–51.

104. Zhu, H.; Kee, R.J.; Janardhanan, V.M.; Deutschmann, O.; Goodwin, D.G. Modeling elementary heterogeneous chemistry and electrochemistry in solid-oxide fuel cells. *J. Electrochem. Soc.* **2005**, *152*, A2427–A2440.

105. Ryu, J.-H.; Lee, K.-Y.; La, H.; Kim, H.-J.; Yang, J.-I.; Jung, H. Ni catalyst wash-coated on metal monolith with enhanced heat-transfer capability for steam reforming. *J. Power Sources* **2007**, *171*, 499–505.

106. Mears, D.E. Diagnostic criteria for heat transport limitations in fixed bed reactors. *J. Catal.* **1971**, *20*, 127–131.